Supporting Information: Deterministic Modelling of Carbon Nanotube Near-Infrared Solar Cells

D.O. Bellisario[§], R.M. Jain[£], Z. Ulissi[‡], M.S. Strano[†,‡]

†Corresponding author: strano@mit.edu
[‡]Department of Chemical Engineering, Massachusetts Institute of Technology, Cambridge, Massachusetts 02139, USA.
[§]Department of Chemistry, Massachusetts Institute of Technology, Cambridge, Massachusetts 02139, USA.
[£]Department of Materials Science & Engineering, Massachusetts Institute of Technology, Cambridge, Massachusetts 02139, USA.

Derivation

Outline of approach and homogeneity approximation

We would like to outline the general methodology to help the reader identify the forest from the trees in the derivation below. The crux of our approach has three sequential elements:

1. Treat single-nanotube properties that are relevant to the network performance as random variables. The priority properties are position, length, orientation, and chirality. The network is defined by the distribution of those parameters.
2. Derive the network behavior from single-SWNT physics as a function of those parameters by performing irradiance, exciton, and free carrier balances. That produces sets of differential equations dependent on the single-SWNT properties.
3. Integrate those differential equations over the distributions of those properties (e.g. integrate over the orientation distribution). That integration is equivalent to summing up the contributions to the balances from each independent population of nanotubes with each possible value of the random variables.

This treatment is only valid under an approximation of macroscopic homogeneity; it implicitly presumes that if you take a slice of the film that is large enough to observe the film's steady state observation, that it will contain the same distribution of properties regardless of where you take the slice. Experimentally, that behavior has been observed with conductivity.[1] That not only constrains our application of the model to films with densities above the percolation threshold, but also excludes cases where the film is highly porous or otherwise exhibits clusters of density, length, chirality, or orientation. It is possible to relax this approximation and treat such cases – see the section *Breakdown of Macroscopic Homogeneity* – but in this work we focus on taking the approximation.

Notation

Bold ($\boldsymbol{v}$) denotes a vector quantity, which may be represented in Cartesian

(1) $$\boldsymbol{v} = \left(v_x, v_y, v_z\right) = v_x\hat{\boldsymbol{x}} + v_y\hat{\boldsymbol{y}} + v_z\hat{\boldsymbol{z}}$$

or spherical

(2) $$\boldsymbol{v} = (r, \theta, \phi), v_x = r\sin\theta\cos\phi\,, v_y = r\sin\theta\sin\phi\,, v_z = r$$

coordinates. We will switch between spherical and Cartesian coordinates for convenience without comment for brevity – which is used should be clear from the context. The space on which a vector is defined varies by context, for example $\boldsymbol{c} = (n_1, n_2)$ is the chirality of a nanotube with chiral indices n_1 and n_2. Hats ($\hat{\boldsymbol{x}}$) denote unite vectors. Subscripts x, y, z will be used to denote the scalar components of a vector in the corresponding Cartesian axis. Unbolded variables (v) corresponding to vectors are the magnitudes of those vectors.

Density functions of a random variable are denoted $p(\cdot)$. Mean values are bracketed as $\langle\cdot\rangle$.

Network Geometry

We consider a network of single-walled nanotubes (SWNT) sandwiched between two electrode plates (Figure 1a). We define a cartesian z axis as perpendicular to the incident solar photon flux J_0 at $z = 0$ (the 'top' of the film), with $z \in \mathbb{R}^+$ being the depth of the film up to thickness T and the film being infinite in cartesian dimensions x and y. In practice the solar flux may be incident at an angle, which would be further altered by the top electrode index of refraction. These considerations merely change the boundary conditions of the light field problem below. The back electrode has reflectance[1] $0 \leq R \leq 1$ which can in general be frequency dependent. A variety of conduction and valence band charge collecting electrode (type II exciton dissociation interface) configurations are possible (Figure 1c), including those

[1] Specular reflectance; we neglect diffuse reflection as a simplification in our treatment.

where an electrode also acts as a photoabsorbing layer (e.g., fullerenes, references [2, 3]). We focus on the relatively general case of two dissociating electrodes (first cartoon in Figure 1c), but the model for the SWNT network applies to any other case by corresponding adjustment of the boundary conditions (next sections). Particular material selection and band alignment issues associated with exciton dissociation are well outside the scope of this work, and instead we take the electrode properties as given.[4]

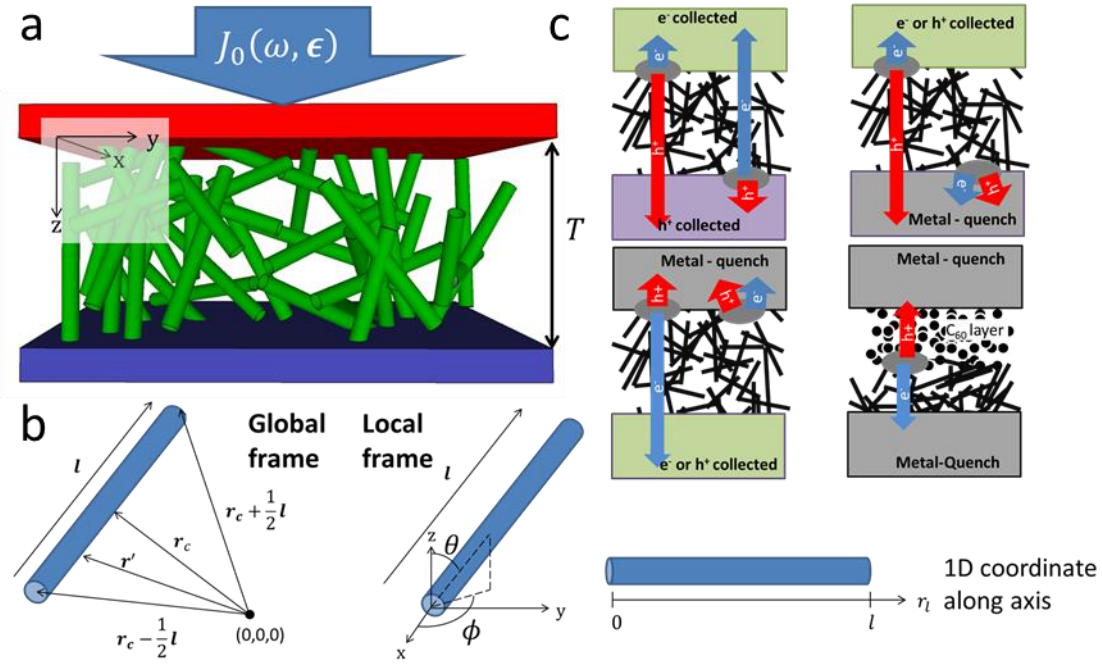

Figure 1. Cartoon of model geometry. See text for description.

Throughout this work we adopt several spatial coordinate references (Figure 1b). An individual nanotube, which we approximate as a rigid rod, has a length and orientation described by the vector in spherical coordinates as $\boldsymbol{l} = (l, \theta, \phi)$, or equivalently in Cartesian coordinates

$$\begin{aligned} \boldsymbol{l} &= (l_x, l_y, l_z) \\ l_x &= l \sin\theta \cos\phi \\ l_y &= l \sin\theta \sin\phi \\ l_z &= l \cos\theta. \end{aligned} \tag{3}$$

In relation to our global coordinate system the center of each nanotube is located at $\boldsymbol{r}_c$ relative to an arbitrary origin in the xy plane at $z = 0$. The ends of a single SWNT are therefore located, relative to the origin, at the ends of vectors $\boldsymbol{r}_c \pm \frac{1}{2}\boldsymbol{l}$. The set of points along the central axis of the SWNT is then constrained as

$$\left\{ \boldsymbol{r}' \middle| \boldsymbol{r}_c + \left(\alpha_l - \frac{1}{2}\right)\boldsymbol{l}, \alpha_l \in [0,1] \right\}. \tag{4}$$

In describing intra-SWNT mechanics we will also consider the one-dimensional space along a nanotube axis, the coordinate along which we will denote $r_l \in [0, l]$. Each r_l corresponds with an $\boldsymbol{r}'$ via $r_l = \alpha_l l$ and Equation (4); there is a bijective map between $\{\boldsymbol{r}'\}$ and $\{r_l\}$. A nanotube also has a chirality $\boldsymbol{c} \equiv (n_1, n_2)$ where n_1 and n_2 are chiral indices.[5] For convenience we index all chiralities present in the network by integer i (chirality $\boldsymbol{c}_i$) in order of increasing exciton (optical) band gap $E_{i+1} > E_i$. The center-center diameter of chirality $\boldsymbol{c}$ is approximately

$$d_{\boldsymbol{c},c-c} \cong \frac{a_0}{\pi}\sqrt{n_1^2 + n_2^2 + n_1 n_2} \tag{5}$$

where $a_0 = 2.461 \times 10^{-10}\ m$ is the graphene lattice constant.[5] The effective outer diameter $d_{\boldsymbol{c}}$ is estimated as the diameter within which the bulk of the electron shell resides, ~0.335 nm greater than $d_{\boldsymbol{c},c-c}$ for tubes with $d_{\boldsymbol{c},c-c} > 0.7\ nm$, based on the thickness of graphene.[6]

The properties $\{\boldsymbol{r}_C, \boldsymbol{l}, \boldsymbol{c}\}$ completely define a given nanotube in our network. Our approach begins with treating these parameters as random variables, defining a given film by their distributions:

$$\begin{aligned} & p(\boldsymbol{r}_C|\boldsymbol{r}) = p\left(r_{cx}, r_{cy}, r_{cz}\middle|\boldsymbol{r}\right) \\ & p(\boldsymbol{l}) = p(l) \cdot p(\theta, \phi) \\ & p(\boldsymbol{c}_i) = v_i \in [0,1], \qquad \sum_i v_i = 1 \end{aligned} \tag{6}$$

where v_i is the number fraction of chirality i in the film. In theory any of the distributions can be dependent on the others depending on the nanotube and film fabrication processes; we focus on cases where they are uncorrelated, but the derivation is general for correlated distributions. We will generate forms of these distributions for different relevant cases – e.g. isotropic, vertically aligned, horizontally aligned, monochiral, mSWNT impurities, short SWNT, long SWNT, etc. when we apply the model to relevant cases (see main paper). Our derivation is also general for cases where all of these properties vary systematically with depth, *i.e.* $p(\boldsymbol{r}_C, \boldsymbol{l}, \boldsymbol{c}|z)$, but in most practical applications $p(\boldsymbol{l})$ and $p(\boldsymbol{c}_i)$ are spatially invariant. Note we are also implicitly assuming that SWNT locations are independent, even though in some film casting processes they can be correlated; this phenomenon represents an important shortcoming of our model, and is discussed further along in the derivation and in the section *Breakdown of Macroscopic Homogeneity*.

Light Field

At any given point $\boldsymbol{r} = (x, y, z) \in \left((-\infty, \infty), (-\infty, \infty), [0, T]\right)$ there is a total photon flux $J_v(\boldsymbol{r})$ that is distributed over (as $J_v(\omega, \boldsymbol{\epsilon}, \boldsymbol{k}|\boldsymbol{r})$, *i.e.* irradiance) frequency ω, linear polarization component $\boldsymbol{\epsilon} = (\theta_\epsilon, \phi_\epsilon)$, and propagation direction $\boldsymbol{k} = (\theta_k, \phi_k)$,[7] i.e.

$$J_v(\boldsymbol{r}) = \int_0^\infty \int_0^\pi \int_0^\pi \int_0^{2\pi} J_v(\omega, \boldsymbol{\epsilon}, \boldsymbol{k}|\boldsymbol{r}) d\phi_\epsilon\, d\theta_\epsilon\, d\theta_k\, d\omega. \tag{7}$$

We do not consider magnetic field effects in this model, although it could be introduced analogously to the electric field if desired subject to $\boldsymbol{b} = \boldsymbol{\epsilon} \times \boldsymbol{k}$. Over our length-scales of interest (< 1 μm) for SWNT material, we neglect electric-field phase shifts such as circular dichroism that introduce and/or manipulate circular polarization components to the light field.

Distributions in polarization and propagation direction of electromagnetic radiation are not independent, they are orthogonal,

$$\boldsymbol{\epsilon} \cdot \boldsymbol{k} = 0, \tag{8}$$

reducing our degrees of freedom by one, leaving only 3 independent dimensions. In practice all four coordinates can be *effectively* taken as independent if proper 'accounting' is done in all the mechanics that follow – i.e. manipulations of the distributions of $\boldsymbol{k}$ are accompanied by appropriate transformation of the distributions of $\boldsymbol{\epsilon}$ and vice versa. Alternatively, that implicit dependency can be made explicit. For example, I take $(\theta_k, \theta_\epsilon, \phi_\epsilon)$ as the independent set, and trigonometrically extract ϕ_k as a function of them:

$$\begin{aligned} \boldsymbol{\epsilon} \cdot \boldsymbol{k} &= 0 \\ &= \epsilon_x k_x + \epsilon_y k_y + \epsilon_z k_z \\ &= \sin\theta_\epsilon \cos\phi_\epsilon \sin\theta_k \cos\phi_k + \sin\theta_\epsilon \sin\phi_\epsilon \sin\theta_k \sin\phi_k \\ &\qquad + \cos\theta_\epsilon \cos\theta_k = 0, \end{aligned} \tag{9}$$

yielding

$$\phi_k(\theta_k, \theta_\epsilon, \phi_\epsilon) = \pi + \phi_\epsilon \pm \operatorname{acos}(\cot\theta_\epsilon \cot\theta_k). \tag{10}$$

As an example of how this basis practically manifests itself, consider a function $F(\boldsymbol{k}) = F(\theta_k, \phi_k)$. We can evaluate its first moment at $\boldsymbol{r}$

$$\begin{aligned} \langle F(\theta_k, \phi_k) \rangle_{\boldsymbol{r}} &= \int_{\boldsymbol{k}} F(\boldsymbol{k})\, J_\nu(\boldsymbol{k}|\boldsymbol{r})\, d\boldsymbol{k} \\ &= \int_0^{\pi} \int_0^{2\pi} F(\theta_k, \phi_k) J_\nu(\theta_k, \phi_k|\boldsymbol{r}) d\phi_k\, d\theta_k \\ &= \int_0^{\pi} \int_o^{\pi} \int_o^{2\pi} F\big(\theta_k, \phi_k(\theta_k, \theta_\epsilon, \phi_\epsilon)\big) J_\nu(\theta_k, \theta_\epsilon, \phi_\epsilon|\boldsymbol{r})\, d\phi_\epsilon\, d\theta_\epsilon d\theta_k \end{aligned} \tag{11}$$

where

$$J_\nu(\theta_k, \theta_\epsilon, \phi_\epsilon|\boldsymbol{r}) = \int_0^{\infty} J_\nu(\omega, \boldsymbol{\epsilon}, \boldsymbol{k}|\boldsymbol{r}) d\omega. \tag{12}$$

The SWNT network can interact with the field through three predominant mechanisms:

1. Absorption, generating excitons of energy $\hbar\omega$.
2. Rayleigh scattering, shifting the distribution of propagation vectors $J_\nu(\boldsymbol{k}|\boldsymbol{r})$.
3. Photoluminescence (PL), radiative decay of excitons to contribute to the photon flux at the energy of the band gap $\hbar\omega_{1u}$, position of the relaxation, and polarization of the transition dipole.

All three phenomena could be included in the derivation that follows, but to first order we neglect the latter two; omitting reflection allows us to remove $\boldsymbol{k}$ from our calculations, and omitting PL greatly simplifies coupling to the exciton transport equations. The former case we will show below, and the latter in the next section. See the *Consideration of Rayleigh Scattering and Photoluminescence* section below for consideration of the consequences of this choice.

To treat attenuation of the field we must derive the linear-polarization- and frequency-dependent absorption cross-section of the film from the single-SWNT absorption behavior. The absorption cross-section of SWNT of chirality $\boldsymbol{c}$ can be broken down as

$$\sigma(\boldsymbol{c}, \boldsymbol{\epsilon}, \omega) = \frac{w(\boldsymbol{c}, \boldsymbol{\epsilon}, \omega)}{J_\nu(\boldsymbol{c}, \boldsymbol{\epsilon}, \omega)} \tag{13}$$

where w is the photon absorption rate at that polarity and frequency, and σ and w are normalized per atom C or mole C (with no length dependence, see references [8, 9]). Theoretical evaluation of absorbance is possible,[10] but given sources of variation, such as dependence on the electric and dielectric environment,[2, 11-13] empirical measurement, $\sigma_{meas}(\boldsymbol{c}, \boldsymbol{\epsilon}, \omega)$,[13-16] is most immediately appealing. Of relevance theoretically is the polarization dependence. A time-dependent perturbation theory treatment of the light-matter interaction yields, to first order under the dipole approximation,[17]

$$\sigma(\boldsymbol{\epsilon}, \omega) \propto \left|\boldsymbol{\epsilon} \cdot \boldsymbol{\mu}_{if}\right|^2 \rho(E_0 + \hbar\omega) \tag{14}$$

where $\boldsymbol{\mu}_{if}$ is the transition dipole between initial and final electronic states, $\langle i|\hat{\boldsymbol{r}}|f\rangle$, E_0 is the energy of ground state $|i\rangle$, and $\rho(E)$ is the density of states at energy E. Electronic transitions in SWNT exist with dipoles parallel and perpendicular to the longitudinal axis (the latter could be called axial as well). The latter set contribute only ~1/5$^{\text{th}}$ of the total absorbance (integrated across all ω), largely due to the depolarization effect.[5, 18]

These transitions provide us with two orthogonal sets of polarization dependence:

$$\sigma\big(\boldsymbol{c}, \boldsymbol{\epsilon}, \hat{\boldsymbol{l}}, \omega\big) \propto \left|\boldsymbol{\epsilon} \cdot \boldsymbol{\mu}_{\parallel}(\boldsymbol{c}, \omega)\right|^2 + |\boldsymbol{\epsilon} \cdot \boldsymbol{\mu}_{\perp}(\boldsymbol{c}, \omega)|^2, \tag{15}$$

where $\boldsymbol{\mu}_{\parallel}$ and $\boldsymbol{\mu}_{\perp}$ are sums of all the dipole moments for transitions of energy $\hbar\omega$ oriented parallel and perpendicular, respectively, to the longitudinal SWNT axis. We therefore effectively have two experimentally- or theoretically-determined absorption cross-section functiona $\sigma_{\parallel}$ and $\sigma_{\perp}$, giving us a total absorption cross-section for a single SWNT of orientation $\hat{\boldsymbol{l}} = (\theta, \phi)$ as

$$\sigma\big(\boldsymbol{c}, \boldsymbol{\epsilon}, \hat{\boldsymbol{l}}, \omega\big) = \left|\boldsymbol{\epsilon} \cdot \hat{\boldsymbol{l}}\right|^2 \sigma_{\parallel}(\boldsymbol{c}, \omega) + \left(1 - \left|\boldsymbol{\epsilon} \cdot \hat{\boldsymbol{l}}\right|\right)^2 \sigma_{\perp}(\boldsymbol{c}, \omega), \tag{16}$$

where the second coefficient has a simple form because both polarization and orientation are unit vectors, and any component of linear polarization not parallel to the SWNT axis is necessarily in the plane perpendicular to it. We will define our coefficients for convenience as

(17) $$\varepsilon_{\parallel}(\theta_{\epsilon},\phi_{\epsilon},\theta,\phi) \equiv \boldsymbol{\epsilon}\cdot\hat{\boldsymbol{l}}$$

(18) $$\varepsilon_{\perp}(\theta_{\epsilon},\phi_{\epsilon},\theta,\phi) \equiv 1-\varepsilon_{\parallel}(\theta_{\epsilon},\phi_{\epsilon},\theta,\phi).$$

In the derivation that follows we will find that normalizing σ per length, σ_l, rather than carbon units is more convenient. For σ per mole of C, as is more usually reported, we can convert readily. The SWNT circumference is

(19) $$2\pi\left(\frac{1}{2}d_{\boldsymbol{c},c-c}\right)=\pi\cdot d_{\boldsymbol{c},c-c},$$

which gives us

(20) $$\frac{1}{N_A}\rho_{graph}\cdot\pi d_{\boldsymbol{c},c-c}$$

moles of carbon per length of SWNT of chirality $\boldsymbol{c}$, where N_A is avogadro's constant and ρ_{graph} is the density of graphene. This relation gives us

(21) $$\sigma_l\left(\boldsymbol{\epsilon},\hat{\boldsymbol{l}},\omega,\boldsymbol{c}\right)=\frac{1}{N_A}\rho_{graph}\cdot\pi d_{\boldsymbol{c},c-c}\cdot\sigma\left(\boldsymbol{\epsilon},\hat{\boldsymbol{l}},\omega,\boldsymbol{c}\right).$$

This conversion is approximate as it neglects bond stress relaxation from curvature, and so measured constants can be used when available; for (6,5) SWNT this estimates 9.1558×10^{10} carbon atoms per length versus 8.8271×10^{10} measured in reference [16].

We can now consider the network. In the remainder of the derivation, two spatial magnifications will be traversed, and the transition between the two will define much of the approach. At the 'macroscopic' scale, $\geq O(100\ nm)$, where the diameter of the nanotubes is negligible, we approximate that the film is essentially homogenous. At the 'microscopic' scale, on the order of $d_{\boldsymbol{c}}$, heterogeneity in the local environment is highly relevant. There are realistic situations where the homogeneity presumption in a strict sense breaks down; the circumstances and impact of that error, as well the means of relaxing the assumption (accounting for macroscopic heterogeneity), are laid out in the section *Breakdown of Macroscopic Homogeneity* below.

From the perspective of the gradient in the light field, the diameter of the SWNT is negligible and the film is essentially homogenous. The length-density of SWNT we will define as the length of SWNT per volume of the film,

(22) $$\rho_{\langle l\rangle}=\int_0^{\infty}\rho\cdot l\cdot p(l)dl=\rho\cdot\langle l\rangle,$$

where ρ is the number density of SWNT and $\langle l\rangle$ is the average length of SWNT. Without any depth-variation in density, the absorption cross-section per volume of film due to SWNT of chirality i and orientation $\hat{\boldsymbol{l}}$ is

(23) $$v_i\cdot\rho_{\langle l\rangle}\cdot\sigma_l\left(\boldsymbol{\epsilon},\hat{\boldsymbol{l}},\omega,\boldsymbol{c}_i\right).$$

where $v_i\rho_{\langle l\rangle}$ can be understood as the density of chirality i in the film. Note that we are omitting explicit dependence on the dielectric environment of each SWNT; that is justifiable under homogeneity if $\sigma_{\parallel}$ and $\sigma_{\perp}$ are measured in or corrected for the appropriate state, but alternatively σ_l can be conditioned on local dielectric constant and integrated over the distribution of it.

A reader familiar with SWNT literature will be more accustomed to seeing quantities liked density expressed in atom or mole Carbon units, rather than by length. That treatment is entirely equivalent to using the length of SWNT, mediated by the carbon atoms per length SWNT, so long as chirality is appropriately accounted for. The per-length quantities however are more useful, as we will see, in translating between one-dimensional and three-dimensional diffusion, where we care about the length of the SWNT present independent of the number of carbon atoms.

For irradiance $J_v(\omega,\boldsymbol{\epsilon},\boldsymbol{k}|\boldsymbol{r})$ the photon absorption rate per volume due to SWNT of chirality i oriented in $\hat{\boldsymbol{l}}$ are

(24) $$N_i\left(\omega, \boldsymbol{\epsilon}, \boldsymbol{k}, \hat{\boldsymbol{l}} | \boldsymbol{r}\right) = v_i \cdot \rho_{\langle l \rangle} \cdot \sigma_l\left(\boldsymbol{\epsilon}, \hat{\boldsymbol{l}}, \omega, \boldsymbol{c}_i\right) \cdot J_v(\omega, \boldsymbol{\epsilon}, \boldsymbol{k} | \boldsymbol{r}).$$

To get the total film absorption rate we must sum absorption terms (24) for nanotubes at each possible orientation $\hat{\boldsymbol{l}}$ and chirality i, weighted by the relative populations of each. That is equivalent however to integrating over the distribution $p(\hat{\boldsymbol{l}})$ (and summing over chiralities), forming the crux of our methodology,

(25)
$$\begin{aligned} N(\omega, \boldsymbol{\epsilon}, \boldsymbol{k} | \boldsymbol{r}) &= \sum_i \int_0^{2\pi} p(\phi) \int_0^{\pi} p(\theta)\, N_i\left(\omega, \boldsymbol{\epsilon}, \boldsymbol{k}, \hat{\boldsymbol{l}} | \boldsymbol{r}\right) d\theta\, d\phi \\ &= \sum_i v_i \int_0^{2\pi} p(\phi) \int_0^{\pi} p(\theta)\, \rho_{\langle l \rangle} \sigma_l\left(\boldsymbol{\epsilon}, \hat{\boldsymbol{l}}, \omega, \boldsymbol{c}_i\right) J_v(\omega, \boldsymbol{\epsilon}, \boldsymbol{k} | \boldsymbol{r})\, d\theta\, d\phi \\ &= \rho_{\langle l \rangle} J_v(\omega, \boldsymbol{\epsilon}, \boldsymbol{k} | \boldsymbol{r}) \sum_i v_i \int_0^{2\pi} p(\phi) \int_0^{\pi} p(\theta)\, \sigma_l\left(\boldsymbol{\epsilon}, \hat{\boldsymbol{l}}, \omega, \boldsymbol{c}_i\right) d\theta\, d\phi \\ &= \rho_{\langle l \rangle} J_v(\omega, \boldsymbol{\epsilon}, \boldsymbol{k} | \boldsymbol{r}) \sum_i v_i \sigma_l(\boldsymbol{\epsilon}, \omega, \boldsymbol{c}_i). \end{aligned}$$

In this manner, we can describe the light interaction behavior of the film by integrating the single-SWNT behavior over the distribution of independent single-SWNT properties. We will take the same approach to exciton and free carrier transport below, where will also consider its utility in more depth. In the last two equalities of (25) we are showing that $\sigma_l(\boldsymbol{\epsilon}, \omega, \boldsymbol{c}_i)$ can be safely evaluated from the film properties before any consideration of absorption, which we exploit in the Results section of the main paper.

Consider a balance on the hypothetical number of photons in a differential volume of the solar cell, $N_P(\boldsymbol{r})$. With absorption as the only light-matter interaction we treat, the change in photons with time is due to absorption events $N(\boldsymbol{r})$ and any gradient in the flux,

(26) $$\frac{dN_p(\omega, \boldsymbol{\epsilon}, \boldsymbol{k} | \boldsymbol{r})}{dt} = -\nabla \cdot J_v(\omega, \boldsymbol{\epsilon}, \boldsymbol{k} | \boldsymbol{r}) - \sum_i N_i(\omega, \boldsymbol{\epsilon}, \boldsymbol{k} | \boldsymbol{r}).$$

At steady state we conveniently lose our $N_p(\boldsymbol{r})$ dependence,

(27) $$\nabla \cdot J_v(\omega, \boldsymbol{\epsilon}, \boldsymbol{k} | \boldsymbol{r}) = -\sum_i N_i(\omega, \boldsymbol{\epsilon}, \boldsymbol{k} | \boldsymbol{r}).$$

We are now in a position to make two useful reductions. First, in the x and y axes where our film is infinite we will treat periodic solutions as trivial, making our boundary conditions in those dimensions

(28)
$$\frac{\partial J_v}{\partial y} = 0$$
$$\frac{\partial J_v}{\partial x} = 0.$$

This simplifies our balance to

(29) $$\frac{dJ(\omega, \boldsymbol{\epsilon}, \boldsymbol{k} | z)}{dz} = -\sum_i N_i(\omega, \boldsymbol{\epsilon}, \boldsymbol{k} | z).$$

Second, neglecting Rayleigh scattering and photoluminescence the $\boldsymbol{k}$ dependence drops out. We can see this by considering the source of incident light, which below we will treat as a boundary condition. Being perpendicularly incident into the film, we have

(30) $$J_v(\theta_k | z = 0) = J_v(z = 0) \cdot \delta(\theta_k - \pi).$$

Without fluorescence or Rayleigh scattering, our balance (Equation (27)) contains no transformations of $\boldsymbol{k}$, and so the initial distribution $J_v(\boldsymbol{k} | z) = J_v(z) \cdot \delta(\theta_k - \pi)$ is maintained. θ_k then trivially integrates out of the balance; for the left hand side we have

(31)
$$\int_0^{2\pi} \nabla J_\nu(\omega, \boldsymbol{\epsilon}|\boldsymbol{r})\delta(\theta_k - \pi)\, d\theta_k = \nabla J_\nu(\omega, \boldsymbol{\epsilon}|\boldsymbol{r}) \int_0^{2\pi} \delta(\theta_k - \pi)\, d\theta_k = \nabla J_\nu(\omega, \boldsymbol{\epsilon}|\boldsymbol{r}),$$

and for the right hand side

(32)
$$\begin{aligned} -\int_0^{2\pi} \sum_i N_i(\omega, \boldsymbol{\epsilon}, \boldsymbol{k}|\boldsymbol{r})\, d\theta_k &= -\sum_i v_i \rho_{\langle l \rangle} \sigma_l\left(\boldsymbol{\epsilon}, \hat{\boldsymbol{l}}, \omega, \boldsymbol{c}_i\right) \int_0^{2\pi} J_\nu(\omega, \boldsymbol{\epsilon}, \boldsymbol{k}|\boldsymbol{r}) d\theta_k \\ &= -\sum_i v_i \rho_{\langle l \rangle} \sigma_l\left(\boldsymbol{\epsilon}, \hat{\boldsymbol{l}}, \omega, \boldsymbol{c}_i\right) J_\nu(\omega, \boldsymbol{\epsilon}|\boldsymbol{r}) \int_0^{2\pi} \delta(\theta_k - \pi)\, d\theta_k \\ &= -\sum_i v_i \rho_{\langle l \rangle} \sigma_l\left(\boldsymbol{\epsilon}, \hat{\boldsymbol{l}}, \omega, \boldsymbol{c}_i\right) J_\nu(\omega, \boldsymbol{\epsilon}|\boldsymbol{r}) \\ &= -\sum_i N_i(\omega, \boldsymbol{\epsilon}|\boldsymbol{r}). \end{aligned}$$

This simplifies our balance to

(33)
$$\nabla \cdot J_\nu(\omega, \boldsymbol{\epsilon}|\boldsymbol{r}) = -\sum_i N_i(\omega, \boldsymbol{\epsilon}|\boldsymbol{r}).$$

Combining the two simplifications, our balance reduces to

(34)
$$\frac{dJ_\nu(\omega, \boldsymbol{\epsilon}|z)}{dz} = -\sum_i N_i(\omega, \boldsymbol{\epsilon}|z).$$

With a transparent back electrode (at $z = T$), the boundary condition can be defined as an incident unpolarized AM1.5 solar flux,

(35)
$$J_\nu(\omega, \boldsymbol{\epsilon}|z = 0) = J_0(\omega, \boldsymbol{\epsilon}).$$

Note that 'unpolarized' is still constrained to be in the incident plane, giving us distributions

(36)
$$J_0(\omega, \theta_{\boldsymbol{\epsilon}}, \phi_{\boldsymbol{\epsilon}}) = J_0(\omega) \cdot \delta\left(\theta_\epsilon - \frac{\pi}{2}\right) \cdot \frac{1}{2\pi}, \qquad \phi_{\boldsymbol{\epsilon}} \in [0, 2\pi]$$

where $J_0(\omega)$ is the AM1.5 solar spectrum. We cannot treat reflection off the back electrode as an alternative boundary condition ($J_\nu'(T) = 0$), as omitting $\boldsymbol{k}$ prevents us from describing the incident flux with a generation term in the balance (34), such as

(37)
$$+J_0(\omega, \boldsymbol{\epsilon}, \boldsymbol{k}) \cdot \delta(z - 0)$$

(38)
$$J_0(\boldsymbol{k}) = J_0(\phi_k) = \delta(\theta_k - \pi).$$

Instead, we recognize that absorption events are independent, allowing us to treat the total light field as the sum of two other fields – one representing the 'forward' flux, $J_F(z)$, and one representing the 'reverse' flux, $J_R(z)$. Interference of incident and reflected light is constrained to a small band of frequencies around harmonics of the film thickness and we therefore neglect it. The fluxes have identical ODEs with opposite generation sign,

(39)
$$\frac{dJ_F(\omega, \boldsymbol{\epsilon}|z)}{dz} = -\sum_i N_i(\omega, \boldsymbol{\epsilon}|z)$$

(40)
$$\frac{dJ_R(\omega, \boldsymbol{\epsilon}|z)}{dz} = \sum_i N_i(\omega, \boldsymbol{\epsilon}|z),$$

but with different boundary conditions. In the forward direction we have the incident solar flux BC, and in the reverse we reflect the forward flux at $z = T$,

(41)
$$J_R(\omega, \boldsymbol{\epsilon}|z = -T) = R \cdot J_F(\omega, \boldsymbol{\epsilon}|z = T),$$

where $R \in [0,1]$ is the reflectivity of the back electrode. Solving the forward and reverse ODEs in sequence, we get the total light field

(42) $$J_\nu(\omega, \boldsymbol{\epsilon}|z) = J_F(\omega, \boldsymbol{\epsilon}|z) + J_R(\omega, \boldsymbol{\epsilon}|z).$$

Integrating over $(\omega, \boldsymbol{\epsilon})$ yields the flux gradient $J_\nu(z)$ and the photon absorption rate $N(z)$.

We should also note that by neglecting $\boldsymbol{k}$ we also complicate treatment of cases where light is not incident along z, i.e. light incident at an angle. In that case we would need to treat not only the longer path length of light both on incidence and reflection, but also we would need to distinguish between the direction that the light gradient is formed along and the direction that excitons diffuse in in the next problem. The situation can be rectified by performing the entire light derivation above not along the dimension z, but along some propagation direction κ with a z component of $\cos\theta_\kappa$. The entire derivation would be the same, except that the gradient in x and y must still be zero, so a 3D balance must be solved to enforce that and extract the gradient in z.

Exciton Transport

In SWNT, optical electronic excitations result in exciton generation – bound carrier states – rather than free charges, due to one dimensional confinement.[12, 19-21] To collect charges in a solar cell, excitons must be dissociated either at a type II interface or by an electric field imparting coulomb force greater than the binding energy. Nonradiative decay of hot excitons to the band gap occurs on a timescale of $O(10\ fs)$;[22, 23] with a longitudinal diffusion coefficient D_l of $O(100\ cm^2/s)$ (see Results section of main paper), the *hot* exciton diffusion length is $< 10\ nm$ and the exponential decay of excited-state energy brings it close to ground state within angstroms. Given that, additionally, the inter-SWNT transport occurs on a timescale of $O(10\ ps)$,[24] we make the key assumption that for $T \gtrsim 10\ nm$, excitons nonradiatively relax to the band gap E_i of the relevant SWNT chirality instantly relative to any other processes we consider. This approximation allows us to neglect hot exciton behavior entirely, and treat the exciton generation rate at band gap energy E_i as the photon absorption rate for chirality i, $N_i(z)$. We further assume that excitons do not interact with free charges, allowing us to couple the two systems only through exciton dissociation. While local dielectric environment – which impacts the exciton diffusion coefficient[25-27] – can be inserted in our model as another random variable without changing the derivation that follows (see *Including Dielectric Environment* section below), we have chosen for simplicity to omit it; for a fairly homogenous dielectric environment, it could be rolled into D_l without much loss of accuracy.

As we will show, a single empirical diffusion coefficient describing exciton transport in a film is limited to *only one* particular geometry and chemistry. Thus, an empirical approach alone would be misguided. Instead, we start with the single-SWNT 1D exciton reaction-diffusion behavior. We then derive the contribution of a network of such systems to three-dimensional exciton transport, and couple them via exciton hopping (EH). The goal is to extract the rate at which excitons arrive and dissociate at the electrodes at $z = \{0, T\}$.The transport is thereby treated in a highly general manner, accommodating for arbitrary network density, co-alignment, net orientation, impurity types and concentrations, length distribution, bundle fraction and size, chirality mixture, and any other properties dependent on the random variables that we used to define the film. There are several ways to approach the coupling problem; the one adopted here was chosen for tractability and generality, but elegant alternatives are mentioned in the section ***Error! Reference source not found.***.

Beginning with a single nanotube of length l, there is a one dimensional coordinate

(43) $$r_l \in [0, l] \text{ or } \alpha_l = \frac{r_l}{l} \in [0,1],$$

with an exciton concentration $n(r_l)$ excitons per length. Excitons are generated at a constant rate $N(r_l)$ that corresponds with an associated $N(\boldsymbol{r}')$ in 3D space from the light absorption problem. In general the exciton concentration is also a function of time, $n(r_l, t)$, but we will be concerned only with steady state operation of the system. We take the excitons to be point particles, i.e. neglecting the finite electron-hole

correlation length. Intra-SWNT exciton transport is diffusive via elastic exciton-phonon scattering.[25, 28-30] This allows us to construct a 1D differential volume balance

$$\frac{dn}{dt} = N(r_l) + D_l \frac{d^2 n}{dr_l^2}, \tag{44}$$

where D_l is the theoretically- or empirically-evaluated longitudinal exciton diffusion coefficient in the dielectric environment of interest (and at the temperature of interest – we focus isothermal operation, see *Relaxing Isothermal Approximation* for how to introduce temperature dependency).[25]

We can then introduce relevant relaxation mechanisms. Radiative (photoluminescent, PL) decay is first order with rate constant $k_\Gamma = 1/\tau_\Gamma$, where τ_Γ is the PL time constant. Exciton quenching from impurities can either be localized via inter-band states allowing nonradiative relaxation (e.g. covalent sp^3-bonded[29, 31] or ionically bonded[30, 32] moieties) or delocalized due to doping.[29] Terms should be included for each species of interest (e.g., oxidative agents, catalyst nanoparticles), with delocalized quenching exhibiting first-order kinetics and localized quenching for an impurity of type im with uniformly distributed concentration distribution n_{im} providing quenching rate

$$-k_{im} n_{im} n(r_l) \tag{45}$$

where k_{im} (in length^2 time^{-1}) is the associated 'bimolecular' rate constant. Note that n_{im} can be understood as the mean number of impurity contacts per length of SWNT; for example if each catalyst nanoparticle on average contacts 3 SWNT, then n_{im} would be three times the film's particle density (number density) divided by the SWNT length density $\rho_{\langle l \rangle}$. Exciton-exciton annhiliation (EEA) via auger recombination is also possible at high fluences,[15, 33-35] yielding the bimolecular reaction term

$$-k_{EEA} \cdot n^2 \tag{46}$$

where k_{EEA} is the rate constant. Following [35] the EEA rate constant can be calculated as

$$k_{EEA} = 128 \frac{\omega_{vc}}{k_{e0}} \left(\frac{\mu}{m_0}\right) \left(\frac{E_{BE}}{E_{11}}\right)^3 \tag{47}$$

where E_{11} is the direct band gap energy, $\mu = m_e m_h/(m_e + m_h)$ is the exciton reduced mass where those masses are the effective masses, $m_e \sim m_h \sim 0.1 m_0$, E_{BE} is the exciton binding energy, m_0 is the free electron mass, ω_{vc} is the interband transition strength, and

$$k_{e0} \equiv \sqrt{\frac{\mu\left(E_g - 2E_{BE}\right)}{\hbar}}. \tag{48}$$

k_{EEA} is approximately $6 \times 10^5\ m/s$ for chiralities in the regime of $E_{BE,i} \cong 0.3\ eV$.[35] Neglecting changes in the exciton coupling potential, we can scale this for different chiralities as

$$k_{EEA}(\boldsymbol{c}_i) = \left(6 \times 10^5 \frac{m}{s}\right) \left(\frac{E_{BE,i}}{E_i}\right)^3 \left(\frac{1.3\ eV}{0.3\ eV}\right)^3. \tag{49}$$

For examinations of single SWNT PL intensities, end quenching is typically taken as a boundary condition.[36, 37] Anticipating expansion to three dimensions however, instead we treat end quenching with another reaction term,

$$-k_{end} \cdot n \cdot \left(\delta(r_l - 0) + \delta(r_l - l)\right) \tag{50}$$

where k_{end} is the end quenching rate constant (length^2 time^{-1}). Our 1D volume balance at steady state then becomes

$$\frac{dn}{dt} = N(r_l) + D_l \frac{d^2 n}{dr_l^2} - k_\Gamma n - k_{EEA} n^2 - \sum_{im} k_{im} n_{im} n - k_{end} n\left(\delta(r_l - 0) + \delta(r_l - l)\right) = 0. \tag{51}$$

To determine the network behavior, we construct a three dimensional volume balance subject to diffusion in one dimensional channels. For clarity we will start with a single chirality in the film and omit index i, bringing in multichiral transport afterwards. We start, as we did in the light absorption case, by focusing on a nanotube population oriented in some direction $\hat{\boldsymbol{l}}$, which will yield a set of differential

equations describing exciton transport; to include terms in those exciton balances for each possible orientation, we will find that we simply need to integrate the ODEs over the orientation distribution $p(\hat{\boldsymbol{l}})$.

For a hypothetical network where all nanotubes lie along the x axis, we have a one dimensional Fick's law exciton flux in a given SWNT, from above, of

(52) $$J_{1D} = -D_l \frac{dn}{dx}.$$

The resulting three-dimensional flux through the x-face (area $dy \cdot dz$) of a differential volume is the product of the one dimensional flux and the number of channels per area. The number of channels per area however is equivalent to the length of SWNT per volume, $\rho_{\langle l \rangle}$, providing a three dimensional flux of

(53) $$J_{3D,x} = \rho_{\langle l \rangle} J_{1D} = -\rho_{\langle l \rangle} D_l \frac{dn}{dx} = -D_l \frac{dc}{dx}$$

where $c(\boldsymbol{r}, t)$ is the exciton concentration per volume and we have exploited homogeneity in the frame of macroscopic diffusion for the relation

(54) $$\rho_{\langle l \rangle} n = c.$$

Note that while Equation (53) has the form of what one would empirically intuit, there is the crucial difference that D_l is exactly the single SWNT exciton diffusion coefficient, not a net film diffusivity; if we had only isolated (uncoupled) SWNT all lying in the x axis then the network diffusivity would be exactly D_l, as one would expect. For a network with orientation distribution $p(\hat{\boldsymbol{l}})$, the diffusion coefficient for each dimension can be broken down by deconvoluting the contributions to the longitudinal diffusivity,

(55) $$D_l = \frac{1}{2} \cdot v_{ex} \cdot l_{mfp}$$

where v_{ex} is the mean exciton velocity, l_{mfp} is the mean free path between elastic exciton-phonon interactions, and the ½ geometric factor reflects the single translation dimension. This relation allows us to infer orientation factors for the longitudinal diffusion coefficient in each dimension,

(56) $$D_{l,x} = \frac{1}{2}(\sin\theta\cos\phi) v_{ex} \cdot (\sin\theta\cos\phi) l_{mfp} = (\sin\theta\cos\phi)^2 D_l$$

(57) $$D_{l,y} = \frac{1}{2}(\sin\theta\sin\phi) v_{ex} \cdot (\sin\theta\sin\phi) l_{mfp} = (\sin\theta\sin\phi)^2 D_l$$

(58) $$D_{l,z} = \frac{1}{2}(\cos\theta) v_{ex} \cdot (\cos\theta) l_{mfp} = (\cos\theta)^2 D_l.$$

Note that (θ, ϕ) are random variables, not Cartesian coordinates, i.e. $\nabla_{\boldsymbol{r}} \cdot f(\theta, \phi) = 0, \forall f$. This yields a diffusion flux in three dimensions of

(59) $$D_l(\sin\theta\cos\phi)^2 \frac{dc}{dx} + D_l(\sin\theta\sin\phi)^2 \frac{dc}{dy} + D_l(\cos\theta)^2 \frac{dc}{dz}$$

Note that diffusion in Equation (59) is only due to longitudinal intra-SWNT transport, we have not yet accounted for exciton hopping (EH) between nanotubes.

Next we extract film quenching kinetics. Radiative decay, being monoexcitonic, remains simply linear in concentration and independent of geometry,

(60) $$-k_\Gamma c.$$

Impurity/defect scattering is similar; multiplying by $\rho_{\langle l \rangle}$ to convert the reaction rate per length of SWNT to rate per volume network

(61) $$-\rho_{\langle l \rangle} \cdot k_{im} n_{im} n = -k_{im} n_{im} c.$$

Treating EEA in the same manner we are left with a lingering n factor remedied by an identity:

(62) $$-\rho_{\langle l \rangle} \cdot k_{EEA} n^2 = -k_{EEA} n \cdot c = -\frac{\rho_{\langle l \rangle}}{\rho_{\langle l \rangle}} \cdot k_{EEA} n \cdot c = -\frac{k_{EEA}}{\rho_{\langle l \rangle}} c^2.$$

Note that we therefore predict an inverse scaling of EEA rate with carbon density, an observation that can be experimentally evaluated. Again note that k_{im} and k_{EEA} are the single SWNT 1D rate constants, *not* empirical film constants, rewarding our microscopic derivation.

Note that in general the quenching rates can be made chirality dependent if desired, just sum and attenuate by chiral fraction, as we did with the absorption cross-section $\sigma(\boldsymbol{c}_i)$ in the light absorption problem, e.g.,

$$-k_\Gamma c \to -\sum_i v_i k_{\Gamma,i} c. \tag{63}$$

Finally we can consider quenching due to the ends of nanotubes. In three dimensions in our homogenous picture an exciton at position $\boldsymbol{r}$ could be on any SWNT of length l, and, constrained by the distribution $p(\boldsymbol{r}_C|\boldsymbol{r})$, could be at any relative distance to the end. As a result, we can treat the SWNT ends as impurities with some concentration, $c_{end}(\boldsymbol{r})$, that is in general non-uniform. For example in a vertically aligned film with one layer of SWNT, there will be more SWNT ends near the two electrodes than in the center of the film (Figure 2b). This can be thought of as the ability to, constrained by $p(\boldsymbol{r}_C|\boldsymbol{r})$, slide SWNT around any point $\boldsymbol{r}$, bringing the end of the SWNT closer or farther away. This observation gives us a rate of end quenching

$$-\frac{k_{end}}{\rho_{\langle l \rangle}} c_{end}(\boldsymbol{r}) \cdot c, \tag{64}$$

where again k_{end} is the one dimensional rate constant. The distribution of end locations $\boldsymbol{r}_{end}$, $c_{end}(\boldsymbol{r}) = p(\boldsymbol{r}_{end}|\boldsymbol{r})$ can either be constructed independently from the film geometry or calculated from the dependency on $p(\boldsymbol{r}_C|\boldsymbol{r})$ and $p(\boldsymbol{l})$ via their relation,

$$\begin{aligned} &\boldsymbol{r}_{end} = \boldsymbol{r}_c \pm \frac{1}{2}\boldsymbol{l} \\ &\Rightarrow p(\boldsymbol{r}_{end}|\boldsymbol{r}_c, \boldsymbol{l}) = \delta\left(\boldsymbol{r}_{end} - \boldsymbol{r}_c + \frac{1}{2}\boldsymbol{l}\right) + \delta\left(\boldsymbol{r}_{end} - \boldsymbol{r}_c - \frac{1}{2}\boldsymbol{l}\right) \\ &c_{end}(\boldsymbol{r}) = p(\boldsymbol{r}_{end}|\boldsymbol{r}) = \int_{\mathbb{R}^3} \int_{\substack{(0,\infty),\\(0,\pi),\\(0,2\pi)}} p(\boldsymbol{r}_{end}|\boldsymbol{r}_c, \boldsymbol{l})\ p(\boldsymbol{r}_c|\boldsymbol{r}) p(\boldsymbol{l}) d\boldsymbol{l} d\boldsymbol{r}_c. \end{aligned} \tag{65}$$

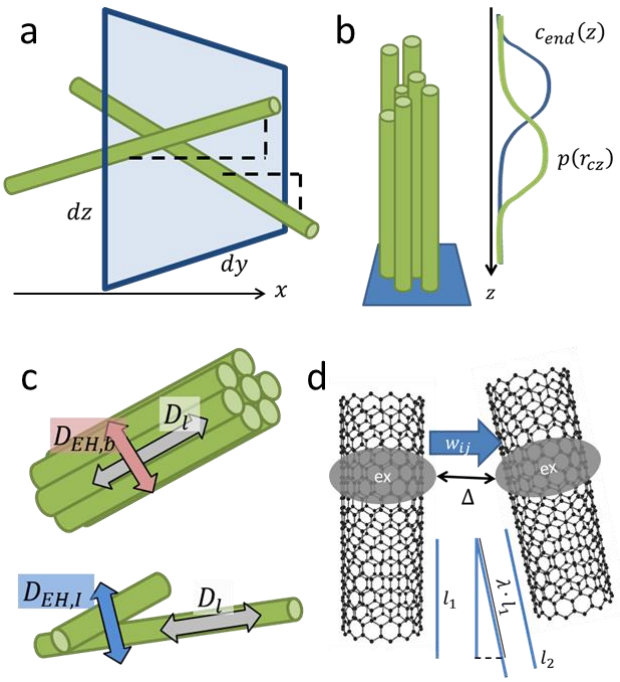

Figure 2. (a) cartoon of nanotubes penetrating the x-face of a differential volume balance. (b) an example cartoon of a vertical SWNT forest demonstrating construction of the SWNT end distribution. (c) illustration of diffusivity perpendicular to longitudinal axis at SWNT intersections and bundles. (d) illustration of tunneling process parameters.

Finally, we consider exciton transport between nanotubes. The mechanisms of exciton transfer/hopping (EH) between nanotubes of the same and different chirality, as well as the mechanisms of type II exciton dissociation at donor-acceptor interfaces, remain under investigation and debate.[3, 4, 38, 39] Explicitly, in the model we treat EH as a tunneling process in bundles and at interconnects, neglecting admittedly vital phenomena such as exciton delocalization[39, 40] and Schottky barriers/band bending.[41] What is important for the future use and evolution of this framework however is that the relevant independent parameters are available, allowing a different functional form to be introduced without contradicting the remainder of the model. This consideration highlights the extensibility of our method beyond our explicit form.

We assume that on our timescale of interest ($O(1\ ps)$) after a transition to a neighboring SWNT an exciton does not maintain momentum in the direction of the transition, yielding random walk character. The result of EH events is therefore a diffusive flux of excitons at inter-SWNT contacts perpendicular to the longitudinal axes (the normal between tubes), a crucial phenomenon for aligned films.[3] For a pair of points $(\boldsymbol{r}_i', \boldsymbol{r}_j')$ on two SWNT of orientations $\hat{\boldsymbol{l}}_i, \hat{\boldsymbol{l}}_j$ with separation (Figure 2d)

(66) $$\Delta \equiv \left|\boldsymbol{r}_i' - \boldsymbol{r}_j'\right| - d_{\boldsymbol{c}}$$

Fermi's golden rule provides a quadratic dependence of the single exciton elastic transition rate w_{EH} on the interaction potential between excitons at the two points, $V_{ij}(\Delta, \hat{\boldsymbol{l}}_i, \hat{\boldsymbol{l}}_j)$:

(67) $$w_{EH} \propto \left|V_{ij}(\Delta, \hat{\boldsymbol{l}}_i, \hat{\boldsymbol{l}}_j)\right|^2.$$

For a tunneling process we anticipate exponential decay of rate with separation [39]

(68) $$\left|V_{ij}(\Delta, \hat{\boldsymbol{l}}_i, \hat{\boldsymbol{l}}_j)\right|^2 \propto e^{-2\beta\Delta}$$

where β (length^{-1}) is the spatial decay constant for the equivalent monoexponential decay of the exciton wave function radially away from the SWNT, e.g.,[2] $\left|\psi_{ex}\right|^2 \propto e^{-2\beta \boldsymbol{r}_\perp}$. The relative alignment of the two SWNT should linearly attenuate the interaction potential by momentum conservation,

(69) $$w_{EH} \propto \left|\hat{\boldsymbol{l}}_i \cdot \hat{\boldsymbol{l}}_j\right|^2.$$

Given the exponential decay of the transition rate and the strong van der Waals attraction between SWNT, we approximate that EH occurs only at intimate SWNT contacts with some fixed $\Delta = \underline{\Delta}$. This approximation allows us to define a fixed proportionality constant k_{EH} such that

(70) $$\lambda \equiv \left|\hat{\boldsymbol{l}}_i \cdot \hat{\boldsymbol{l}}_j\right|$$

(71) $$w_{EH} = k_{EH}\lambda^2.$$

k_{EH} can be determined experimentally or from theoretical evaluation.

From the transition rate at contacts we can derive the resulting diffusion coefficients. In the 1D axis along the transition direction (perpendicular to both SWNT longitudinal axes $\hat{\boldsymbol{l}}_i, \hat{\boldsymbol{l}}_j$, i.e. $\hat{\boldsymbol{l}}_i \times \hat{\boldsymbol{l}}_j$) the diffusivity can be expressed as a product of the velocity and mean free path as in Equation (55). Since each transition covers the effective distance $\underline{\Delta} + d_{\boldsymbol{c}}$ and are independent events, the effective velocity is $w_{EH}(\underline{\Delta} + d_{\boldsymbol{c}})$ and mean free path is $\underline{\Delta} + d_{\boldsymbol{c}}$, giving us

(72) $$D_{EH} = \frac{1}{2} \cdot w_{EH}(\underline{\Delta} + d_{\boldsymbol{c}}) \cdot (\underline{\Delta} + d_{\boldsymbol{c}}) = \frac{1}{2} k_{EH}\lambda^2 (\underline{\Delta} + d_{\boldsymbol{c}})^2.$$

The network diffusion resulting from this transport at contacts is intimately dependent on the microscopic heterogeneity of the film; both the co-alignment and contact density (correlated position) distributions, rather than mean values, determine the resulting film EH diffusivity. For example, a film comprised entirely of bundles – which have large contact areas and near-perfect alignment – will exhibit enhanced EH diffusion relative to an isotropic film. As another example, recalling the *Breakdown of Macroscopic*

[2] For a square tunneling barrier between SWNT this is rigorous, but in practice even with no interstitial contaminants the image potential in each SWNT gives curvature to the tunneling barrier. The wavefunction decay therefore won't be exactly monoexponential, but will always be rapid.

Homogeneity section, a network with larger voids (at the same total density) will exhibit more efficient EH transport due to higher correlation of positions (and therefore a higher density of contacts).

We divide the film into two distinct microscopic environments: bundles and interconnects. The bundling coefficient, b_c, we define as the length fraction of SWNT in bundles. Along with the mean number of SWNT in a bundle, M_b, we can determine the diffusivity due to bundling (again, neglecting exciton delocalization[39]). In a close-packed bundle, a single SWNT can be surrounded by anywhere from 1 to 6 neighbors, and each neighbor of the same chirality provides the pairwise diffusion pathway described in (72). For χ nearest neighbors around each SWNT, and $\lambda = 1$ in bundles, the diffusivity in the plane perpendicular to the bundle would be

$$D_{EH,b} = \chi \frac{1}{4} k_{EH,b} (\Delta_B + d_c)^2. \tag{73}$$

If we define χ_i as the probability of a member of the bundle having i neighbors, then we can determine χ as

$$\chi = \sum_{i=1}^{6} i \cdot \chi_i. \tag{74}$$

We can calculate the mean value of χ from only the average bundle size. As $M_B \to \infty, \chi \to 6$, giving us a functional form (with constants n and Q)

$$\chi(M_B) = \frac{6 \cdot M_B^n - Q}{M_B^n}. \tag{75}$$

At a minimum bundle size of 2 we must have $\chi = 1$, giving us

$$\chi(2) = 1 \to Q = 5 \cdot 2^n. \tag{76}$$

From the series of maximal $\chi(M_B)$ we can evaluate n as ~0.51,

$$\chi(M_B) = \frac{6 \cdot M_B^{0.51} - 5 \cdot 2^{0.51}}{M_B^{0.51}}. \tag{77}$$

With diffusivity $D_{EH,b}$ (Equation (73)) in the plane perpendicular to a bundle, we have the resulting exciton flux in Cartesian coordinates

$$\begin{aligned} &b_c(1 - \sin\theta\cos\phi)^2 D_{EH,b} \frac{dc}{dx} + b_c(1 - \sin\theta\sin\phi)^2 D_{EH,b} \frac{dc}{dy} \\ &+ b_c(1 - \cos\theta)^2 D_{EH,b} \frac{dc}{dz} \end{aligned} \tag{78}$$

Outside of bundles, exciton transport between nanotubes is still expected at interconnects between SWNT. The resulting flux will in general be lower than bundled SWNT EH due to 1) imperfect alignment ($\lambda < 1$) and 2) lower overlap lengths (in bundles the entire length of the SWNT overlap, giving $b_c \rho_{\langle l \rangle}$ length of SWNT in bundles per volume, whereas at interconnects only a small region of length $\sim d_c$ is contacted between SWNT.

An ideal treatment of the number of SWNT contacts per volume would include the correlation of nanotube locations, for example by deriving it from the nanotube radial distribution function (See section *Breakdown of Macroscopic Homogeneity* below). As discussed in that section however, a good first approximation is to assume an independent dispersion (i.e. uniform distribution). We can determine the density of interconnects by considering a control volume surrounding a nanotube of length l (Figure 3).

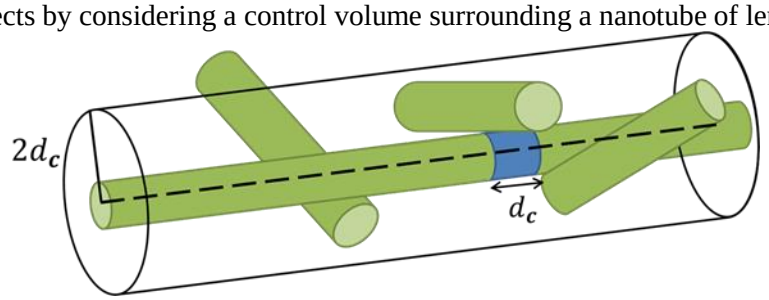

Figure 3. Cartoon of a control volume around an unbundled nanotube.

The number of other SWNT with central axes in the volume up to d_c away is the number of interconnects in the control volume (whether the locations are correlated or not, see *Breakdown of Macroscopic Homogeneity*). In other words, the number of contacts is the number of other nanotubes within one diameter of the control nanotube. To roughly approximate the bending ability of the nanotubes (deviation from rigid rods) the contact distance can be extended to twice the mean displacement r_{bend}

(79) $$d_c + 2r_{bend},$$

for example an additional $\sim d_c$. The volume excluding the central nanotube is then

(80) $$l\left(\pi(2d_c)^2 - \pi\left(\frac{d_c}{2}\right)^2\right) = l\frac{15}{4}\pi d_c^2.$$

In that volume there are, based on the number of SWNT per volume ρ,

(81) $$\left(1 - b_c\left(1 - \frac{1}{M_B}\right)\right)\rho \cdot l\frac{15}{4}\pi d_c^2$$

other SWNT present, accounting for SWNT pulled into bundles.[3] This yields the number of intersections per length of the control nanotube,

(82) $$\begin{aligned} n_I &= \frac{1}{l}\cdot\left(1 - b_c\left(1 - \frac{1}{M_B}\right)\right)\rho \cdot l\frac{15}{4}\pi d_c^2 \\ &= \left(1 - b_c\left(1 - \frac{1}{M_B}\right)\right)\rho\frac{15}{4}\pi d_c^2. \end{aligned}$$

Multiplying by the length of SWNT not in bundles per volume we have

(83) $$\begin{aligned} &\left(1 - b_c\left(1 - \frac{1}{M_B}\right)\right)\rho_{\langle l\rangle}\cdot\left(1 - b_c\left(1 - \frac{1}{M_B}\right)\right)\rho\frac{15}{4}\pi d_c^2 \\ &= \rho_{\langle l\rangle}\rho\left(1 - b_c\left(1 - \frac{1}{M_B}\right)\right)^2\frac{15}{4}\pi d_c^2 \end{aligned}$$

intersections per volume of solar cell. If each intersection to provides $\sim d_c$ of contact length along the SWNT, the length of intersections per volume is

(84) $$\rho_{\langle l\rangle}\rho\left(1 - b_c\left(1 - \frac{1}{M_B}\right)\right)^2\frac{15}{4}\pi d_c^3.$$

For each intersection, we have the diffusivity expression (72),

(85) $$D_{EH,I} = \frac{1}{2}k_{EH}\lambda^2\left(\underline{\Delta} + d_c\right)^2,$$

providing a flux in the dimension along the intersection $\hat{\boldsymbol{l}}_i \times \hat{\boldsymbol{l}}_j$

(86) $$J_{EH,I,\hat{\boldsymbol{l}}_i\times\hat{\boldsymbol{l}}_j} = D_{EH,I}\frac{dn}{dx}.$$

Multiplying by the number of intersections in a cross-sectional area we arrive at the film fluxes arising from interconnects,

(87) $$J_{EH,I,x} = (1 - \sin\theta\cos\phi)^2\cdot\rho\left(1 - b_c\left(1 - \frac{1}{M_B}\right)\right)^2\frac{15}{4}\pi d_c^3\cdot D_{EH,I}\frac{dc}{dx}$$

(88) $$J_{EH,I,y} = (1 - \sin\theta\sin\phi)^2\cdot\rho\left(1 - b_c\left(1 - \frac{1}{M_B}\right)\right)^2\frac{15}{4}\pi d_c^3\cdot D_{EH,I}\frac{dc}{dy}$$

(89) $$J_{EH,I,z} = (1 - \cos\theta)^2\cdot\rho\left(1 - b_c\left(1 - \frac{1}{M_B}\right)\right)^2\frac{15}{4}\pi d_c^3\cdot D_{EH,I}\frac{dc}{dz}$$

where the leading trigonometric terms are again projections onto the plane perpendicular to the control nanotube longitudinal axis, and we employed relation (54). To account for significant reductions in inter-

[3] i.e. each bundle itself can behave as a nanotube, providing the $\left(1 - \frac{1}{M_B}\right)$ coefficient.

SWNT contacts arising from nanotube coatings (e.g., polymer, surfactant), an interstitial modifier A_I can be included to attenuate the number of interconnects with the proportional factor $1 - A_I$,

$$J_{EH,I,x} = (1 - A_I) \cdot (1 - \sin\theta\cos\phi)^2 \cdot \rho \left(1 - b_c\left(1 - \frac{1}{M_B}\right)\right)^2 \frac{15}{4}\pi d_c^3 \cdot D_{EH,I}\frac{dc}{dx}$$

(90)
$$J_{EH,I,y} = (1 - A_I) \cdot (1 - \sin\theta\sin\phi)^2 \cdot \rho \left(1 - b_c\left(1 - \frac{1}{M_B}\right)\right)^2 \frac{15}{4}\pi d_c^3 \cdot D_{EH,I}\frac{dc}{dy}$$

$$J_{EH,I,z} = (1 - A_I) \cdot (1 - \cos\theta)^2 \cdot \rho \left(1 - b_c\left(1 - \frac{1}{M_B}\right)\right)^2 \frac{15}{4}\pi d_c^3 \cdot D_{EH,I}\frac{dc}{dz}.$$

This adjustment is not necessary in bundles, as the definition of the bundle coefficient explicitly rejects lengths of SWNT that are not in intimate contact.

The final consideration in exciton diffusion at contacts is the co-alignment (λ) dependence. Since no other term in our balance will depend on the relative orientation,

(91) $$\lambda \equiv \left|\hat{\boldsymbol{l}}' \cdot \hat{\boldsymbol{l}}''\right| = \lambda(\theta', \theta'', \phi', \phi''),$$

integrating over $p(\lambda)$ yields

(92) $$D_{EH,I} = \frac{1}{2}k_{EH}\left(\underline{\Delta} + d_c\right)^2 \cdot \langle\lambda^2\rangle.$$

$\langle\lambda^2\rangle$ is readily calculable given the distribution of $p(\hat{\boldsymbol{l}})$. For example two methods would be:

1) Integrate λ^2 over the distribution of angles directly

(93) $$\langle\lambda^2\rangle = \int\int\int\int \lambda^2 p(\theta')p(\theta'')p(\phi')p(\phi'')d\theta' d\theta'' d\phi' d\phi''$$

2) Evaluate the product distribution

(94) $$p(\lambda|\theta', \theta'', \phi', \phi'') = \delta\left(\lambda - \left|\hat{\boldsymbol{l}}' \cdot \hat{\boldsymbol{l}}''\right|\right)$$

(95)
$$\begin{aligned}\left|\hat{\boldsymbol{l}}' \cdot \hat{\boldsymbol{l}}''\right| &= l_x' \cdot l_x'' + l_y' \cdot l_y'' + l_z' \cdot l_z'' \\ &= |\sin\theta'\cos\phi'\sin\theta''\cos\phi'' \\ &\quad + \sin\theta'\sin\phi'\sin\theta''\sin\phi'' + \cos\theta'\cos\theta''|\end{aligned}$$

(96)
$$\begin{aligned}p(\lambda) &= \int_0^{2\pi}\int_0^{2\pi}\int_0^{\pi}\int_0^{\pi} p(\lambda|\theta', \theta'', \phi', \phi'')p(\theta')p(\theta'')p(\phi')p(\phi'')d\theta' d\theta'' d\phi' d\phi''.\end{aligned}$$

The expected value is then

(97) $$\langle\lambda^2\rangle = \int_0^1 \lambda^2 p(\lambda)d\lambda.$$

Including all three diffusion mechanisms, the volume balance for exciton transport in a monochiral network is

(98) $$Let\ \gamma_I \equiv \rho\left(1 - b_c\left(1 - \frac{1}{M_B}\right)\right)^2 \frac{15}{4}\pi d_c^3 = \left(1 - b_c\left(1 - \frac{1}{M_B}\right)\right) d_c \cdot n_I$$

$$\frac{dc}{dt} = N(\boldsymbol{r}) + \Big(D_l(\sin\theta\cos\phi)^2 + (1-\sin\theta\cos\phi)^2\left((1-A_I)\gamma_I D_{EH,I} + b_c D_{EH,b}\right)\Big)\frac{d^2c}{dx^2} + \Big(D_l(\sin\theta\sin\phi)^2 + (1-\sin\theta\sin\phi)^2\left((1-A_I)\gamma_I D_{EH,I} + b_c D_{EH,b}\right)\Big)\frac{d^2c}{dy^2} + \Big(D_l(\cos\theta)^2 + (1-\cos\theta)^2\left((1-A_I)\gamma_I D_{EH,I} + b_c D_{EH,b}\right)\Big)\frac{d^2c}{dz^2} - k_\Gamma c - c\sum_{im} k_{im} n_{im} - \frac{k_{EEA}}{\rho_{\langle l\rangle}}c^2 - \frac{k_{end}}{\rho_{\langle l\rangle}}c_{end}(\boldsymbol{r})\cdot c. \tag{99}$$

We can recognize γ_I as representing the 'sparsity' influence on orthogonal diffusivity, with $\gamma_I \to 0$ for a fully-bundled film (independent of density). Analogously to the light field balance, we can recognize that periodic results in x and y are trivial, simplifying the balance to the z coordinate,

$$\frac{dc}{dx} = \frac{dc}{dy} = 0 \tag{100}$$

$$\frac{dc}{dt} = N(z) + \Big((\cos\theta)^2 D_l + (1-\cos\theta)^2\left((1-A_I)\gamma_I D_{EH,I} + b_c D_{EH,b}\right)\Big)\frac{d^2c}{dz^2} - k_\Gamma c - c\sum_{im} k_{im} n_{im} - \frac{k_{EEA}}{\rho_{\langle l\rangle}}c^2 - \frac{k_{end}}{\rho_{\langle l\rangle}}c_{end}(z)\cdot c. \tag{101}$$

The balance is subject to steady state conditions and electrode boundary conditions, treated below. For simplicity we can now define a total network diffusion coefficient,

$$D_{tot} \equiv (\cos\theta)^2 D_l + (1-\cos\theta)^2\left((1-A_I)\gamma_I D_{EH,I} + b_c D_{EH,b}\right). \tag{102}$$

Analogous to the light absorption problem, we have constructed a differential equation describing exciton transport due to nanotubes with orientation $\hat{\boldsymbol{l}}$, but to get the total balance we must sum contributions from all possible orientations. Again, that weighted sum is equivalent to integrating (102) over the distribution $p(\hat{\boldsymbol{l}})$. This treatment is only valid under our approximation of a homogenous film. That is our method: **treat single-SWNT chemical and geometric parameters as random variables, derive network behavior from single-SWNT physics as a function of those parameters, and finally integrate the solution over the distribution of those parameters**. In the *Results* section we illustrate this process when we apply it to specific cases.

This is an important result; equation (101) has the intuitive reaction-diffusion form one might guess for an empirical fit of a given experimental solar cell, but

A) the net diffusivity D_{tot} and several of the kinetic rate constants depend exquisitely on the film properties ($p(\hat{\boldsymbol{l}}), \rho_{\langle l\rangle}, p(l)$), preventing broader applicability of any single diffusivity measurement, and
B) by considering the distributions of single-SWNT parameters and the microscopic mechanisms of exciton transport and decay, we have been able to derive the dependence of network diffusion and reaction constants on film properties and fundamental single-exciton physical constants.

Furthermore, this framework built on treating single-SWNT parameters as random variables and defining the network through their distributions is flexible and adaptive; particular terms – such as exciton hopping diffusivities – can be changed as SWNT exciton physics is better understood. New parameters with associated distributions can be introduced, such as dielectric constant and local density (radial distribution function), and variable independence assumptions can be relaxed, increasing complexity and nuance without grossly deteriorating numerical solvency.

Multiple chiralities can now be introduced. Separate balances can be constructed for excitons residing on each chirality, $c_i(z)$, coupled by inter-SWNT interactions (exciton hopping, limited by band

gap alignment rules). In applying the model we make the simplifying assumptions of homogenous chirality distributions (v_i independent of z), and chirality-independent length and orientation distributions; all of those assumptions can be relaxed without invalidating the remaining derivation. The total concentration of excitons is thus

(103) $$c_i = v_i c$$

(104) $$c(\boldsymbol{r}) = \sum_{i\in\{\boldsymbol{c}_i\}} c_i(\boldsymbol{r}) = c(\boldsymbol{r}) \sum_{i\in\{\boldsymbol{c}_i\}} v_i = c(\boldsymbol{r}).$$

Beginning with quenching due to metallic nanotubes (mSWNT), we denote v_m as the mSWNT fraction. Since nonradiative quenching on mSWNT is rapid compared to residence times, we do not need to construct a concentration balance for them, and the impact of EH to mSWNT is an exciton loss term for all other chiralities. Along the length of an unbundled SWNT every contact with mSWNT quenches excitons at rate

(105) $$k_{EH}\langle\lambda^2\rangle \cdot n.$$

The length of intersection per length SWNT is the intersections per length times the length of each intersection,

(106) $$n_{I,m} \cdot d_{\boldsymbol{c}},$$

where $n_{I,m}$ is the number of intersections with a metal SWNT per length SWNT, which is related to our earlier quantity n_I number of intersections total per length SWNT (Equation (82)) via

(107) $$n_{I,m} = v_m n_I = v_m \left(1 - b_c\left(1 - \frac{1}{M_B}\right)\right)\rho\frac{15}{4}\pi d_{\boldsymbol{c}}^2.$$

Multiplying the rate per intersection times the length of intersection per length SWNT gives the total quenching rate for a single-nanotube 1D system

(108) $$-k_{EH}\langle\lambda^2\rangle \cdot v_m n_I \cdot d_{\boldsymbol{c}} \cdot n.$$

We extend to the film quenching rate by multiplying by the length of unbundled mSWNT per cell volume,

(109)
$$\begin{aligned} &-\left(1 - b_c\left(1 - \frac{1}{M_B}\right)\right)\rho_{\langle l\rangle} \cdot k_{EH}\langle\lambda^2\rangle \cdot v_m n_I \cdot d_{\boldsymbol{c}} \cdot n \\ &= -\left(1 - b_c\left(1 - \frac{1}{M_B}\right)\right) \cdot k_{EH}\langle\lambda^2\rangle \cdot v_m n_I \cdot d_{\boldsymbol{c}} \cdot c \\ &= -k_{EH}\langle\lambda^2\rangle \cdot v_m \gamma_I c \end{aligned}$$

where in the final equality we substitute in definition (98).

Note that $d_{\boldsymbol{c}}$ varies by chirality, making the relevant control volume chirality-dependent; properly, the coupling term for EH to/from chirality *j* at interconnects in the balance of excitons on chirality *i* should have in Equation (80) $d_{\boldsymbol{c}} \to \left(d_{\boldsymbol{c},i} + d_{\boldsymbol{c},j}\right)$ in the first term $d_{\boldsymbol{c},i}$ in the second term, i.e.

(110) $$l\left(\pi\left(d_{\boldsymbol{c},i} + d_{\boldsymbol{c},j} + 2r_{bend}\right)^2 - \pi\left(\frac{d_{\boldsymbol{c},i}}{2}\right)^2\right).$$

For practical purposes however when diameters are similar the effect is small compared to r_{bend}.

To treat mSWNT quenching in bundles, consider the number of mSWNT per cross-sectional area of a bundle,

(111) $$v_m \cdot \frac{2}{\sqrt{3}} d_{\boldsymbol{c}}^{-2}.$$

By definition of the diffusion coefficient, excitons in a cross-section cover $D_{EH,b}$ area per time, yielding an exciton quenching rate (mean rate of arrival to a mSWNT) of

(112) $$-D_{EH,b} \cdot v_m \cdot \frac{2}{\sqrt{3}} d_{\boldsymbol{c}}^{-2} \cdot n$$

per length of SWNT. Multiplying by the length of SWNT in bundles per volume yields the film quenching rate due to mSWNT in bundles

(113) $$-b_c\rho_{\langle l\rangle} \cdot D_{EH,b} v_m \frac{2}{\sqrt{3}} d_{\boldsymbol{c}}^{-2} \cdot n = -b_c \cdot D_{EH,b} v_m \frac{2}{\sqrt{3}} d_{\boldsymbol{c}}^{-2} \cdot c.$$

We can now construct exciton concentration balances for each chirality, $c_i(z)$. In addition to all of the monochiral balance (101) and mSWNT quenching terms ((109) and (113)), the balances for each chirality are coupled to one another through EH interactions in bundles and interconnects. Recall that we have chosen indices such that band gap ($E_i \equiv E_{1u,i}$) and index are monotonically increasing ($E_{i+1} > E_i$). Because transitions are elastic, exciton transitions from higher bandgaps to lower bandgaps occur at rates analogous to mSWNT quenching; transitions 'up' bandgaps may be thermally activated for small band gaps, in which case they are attenuated by an Aarhenius factor,

$$j > i, \qquad k_{EH} \to k_{EH} e^{-\frac{E_j - E_i}{k_B T}}. \tag{114}$$

In the balance for chirality i, we have exciton loss due to unbundled coupling, [4]

$$-c_i \sum_{j<i} \left(1 - b_c \left(1 - \frac{1}{M_B}\right)\right) k_{EH} \langle \lambda^2 \rangle \cdot v_j n_I \cdot d_{\boldsymbol{c}} = -c_i \sum_{j<i} k_{EH} \langle \lambda^2 \rangle \cdot v_j \gamma_I \,, \tag{115}$$

exciton gain due to unbundled coupling,

$$+\sum_{j>i} \left(1 - b_c \left(1 - \frac{1}{M_B}\right)\right) k_{EH} \langle \lambda^2 \rangle \cdot v_j n_I \cdot d_{\boldsymbol{c}} \cdot c_j = +\sum_{j>i} k_{EH} \langle \lambda^2 \rangle \cdot v_j \gamma_I \cdot c_j, \tag{116}$$

exciton loss due to bundled coupling,

$$-c_i \sum_{j<i} b_c \cdot D_{EH,b} v_j \frac{2}{\sqrt{3}} d_{\boldsymbol{c}}^{-2} \,, \tag{117}$$

and exciton gain due to bundled coupling,

$$+\sum_{j<i} b_c \cdot D_{EH,b} v_j \frac{2}{\sqrt{3}} d_{\boldsymbol{c}}^{-2} \; c_j. \tag{118}$$

Note again that we are neglecting band bending and Schottky barriers at the interfaces of SWNT, which may play a significant role in transition rates;[4, 41] as understanding of such phenomena is reached, the coupling expressions (115)-(118) can be changed appropriately.

The final expression for multichiral network exciton transport is then the system of ordinary differential equations

[4] For clarity of presentation and because the effects can be small, I have not included the thermally excited transition terms. They are identical to the terms presented, but with the opposite sum inequality and an Aarhenius prefactor in line with (114). For example, in Equation (145) the term would be

$$-c_i \sum_{j>i} e^{-\frac{E_j - E_i}{k_B T}} \cdot \left(1 - b_c \left(1 - \frac{1}{M_B}\right)\right) k_{EH} \langle \lambda^2 \rangle \cdot v_j n_I \cdot d_{\boldsymbol{c}}$$

$$\begin{aligned}\frac{dc_i}{dt} = v_i N(z) + D_{tot}\frac{d^2c_i}{dz^2} - k_\Gamma c_i - c_i\sum_{im} k_{im}n_{im} - \frac{k_{EEA}}{\rho_{\langle l\rangle}}c_i^2 \\ - \frac{k_{end}}{\rho_{\langle l\rangle}}c_{end}(z)\cdot c_i - k_{EH}\langle\lambda^2\rangle\cdot v_m\gamma_I c_i \\ - b_c D_{EH,b} v_m \frac{2}{\sqrt{3}} d_{\boldsymbol{c}}^{-2}\cdot c_i \\ - c_i\sum_{j<i}\left(k_{EH}\langle\lambda^2\rangle\cdot v_j\gamma_I + b_c\cdot D_{EH,b}v_j\frac{2}{\sqrt{3}}d_{\boldsymbol{c}}^{-2}\right) \\ + \sum_{j>i} c_j\cdot\left(k_{EH}\langle\lambda^2\rangle\cdot v_j\gamma_I + b_c\cdot D_{EH,b}v_j\frac{2}{\sqrt{3}}d_{\boldsymbol{c}}^{-2}\right)\end{aligned} \tag{119}$$

for each chirality i.

The system of ODEs (119) can be solved at steady state subject to boundary conditions at the electrodes ($z = 0, T$). A variety of electrode configurations can be considered (Figure 1c); in proceeding we focus on two electrodes that can drive type II exciton dissociation – one hole accepting and one electron accepting. For each electrode we therefore have Robin boundary conditions from the exciton splitting rate,

$$\left.\frac{dc_i}{dz}\right|_{z=0} = \frac{k_{d0,i}}{D_{tot}}c_i(z=0) \tag{120}$$

$$\left.\frac{dc_i}{dz}\right|_{z=T} = -\frac{k_{dT,i}}{D_{tot}}c_i(z=T). \tag{121}$$

where $k_{d0,i}$ and $k_{dT,i}$ are the dissociation rate constants that in general could depend on the chirality i. In applying the model in this work we approximate perfect collection efficiency, i.e. $k_{d0}, k_{dT} \to \infty$, $c_i(z = 0, T) \to 0$, and check convergence to a finite value of $k_{d0,dT}c(z = 0, T)$.

Charge Transport

Free carrier transport in the nanotube network is in many ways more challenging than exciton diffusion. In addition to the analogous geometric effects on film charge mobility and diffusivity, charge transfer at the interface of nanotubes, particularly of different chiralities, can block or trap charges.[41] Asymmetric electron and hole generation (at the two electrodes) and slow mobilities can lead to an electric field development that feeds back on the exciton dissociation problem, inhibiting dissociation and/or driving spontaneous in-film dissociation when the field strength exceeds the binding energy. Finally carrier densities can significantly impact mobility.[42]

In this work we do not seek to accurately describe free carrier transport in the SWNT film. Rather, we proceed under the large simplification that performance will be limited by exciton diffusion, due to high longitudinal mobilities in any intrinsic electric field.[42] This assumption reduces coupling between the free carrier and exciton problems to the exciton dissociation rate. We also continue to neglect any charge-transfer effects at inter-SWNT contacts, as those effects have been neither theoretically nor experimentally defined. These rough assumptions allow, as we show, important results in the optimization of film performance, but prohibit accurate quantitative prediction of external quantum efficiency (EQE). In future work, we will develop a more complete consideration of free carrier transport.

A variety of electrode materials and configurations are possible (Figure 1c), the choice of which impacts charge carrier transport profoundly, just as in any excitonic photovoltaic system. In this work we focus on an illustrative case of one electron-collecting and one hole-collecting electrode, arbitrarily choosing $z = 0$ to be electron-collecting (Figure 4).

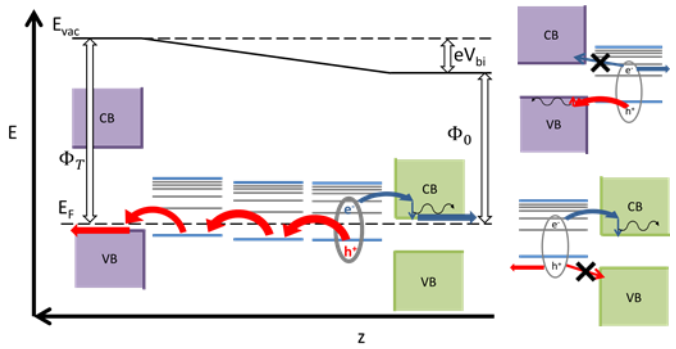

Figure 4. cartoon of the free carrier generation and translation process at the electron-collecting electrode, where band alignment is chosen such that holes are blocked and electron relaxation in the electrode conduction band compensates for the binding energy of the nanotube. Intrinsic work function differences between the two electrodes inspire a potential drop of $\Phi_T - \Phi_0$.

We estimate the geometric impact on valence and conduction band carrier mobilities in the film from the exciton behavior. We attenuate single-SWNT electron and hole mobilities, μ_e^* and μ_h^*, by the network attenuation of single-SWNT exciton diffusivities,

(122) $$D_e = D_e^* \frac{D_l}{D_{tot}} = \mu_e^* \frac{k_B T}{q} \frac{D_{tot}}{D_l}$$

(123) $$D_h = D_h^* \frac{D_l}{D_{tot}} = \mu_h^* \frac{k_B T}{q} \frac{D_{tot}}{D_l}$$

where we have applied the Einstein relation at low bias, q is the elementary charge, k_B is Boltzmann's constant, and (here only) T is the isothermal film temperature. Reversing the Einstein relation we extract the film mobilities,

(124) $$\mu_e = \frac{q}{k_B T} D_e$$

(125) $$\mu_h = \frac{q}{k_B T} D_h.$$

We now balance the non-equilibrium populations of conduction band carriers, $f_e(\boldsymbol{r})$, and valence band carriers, $f_h(\boldsymbol{r})$, which are coupled to one another and the electric field $\mathcal{E}_z(z)$. We again identify that in any practical case

(126) $$\frac{df_e}{dx} = \frac{df_e}{dy} = \frac{df_h}{dx} = \frac{df_h}{dy} = 0$$

and our problem is confined to the z axis. For each carrier there are drift and diffusion fluxes,

(127) $$J_e^{diff} = -D_e \frac{df_e}{dz}$$

(128) $$J_e^{drift} = -\mu_e \mathcal{E}_z \cdot f_e$$

(129) $$J_h^{diff} = -D_h \frac{df_h}{dz}$$

(130) $$J_h^{drift} = \mu_h \mathcal{E}_z \cdot f_h.$$

The fluxes contribute to a population balance on a differential volume as

(131) $$\frac{df_e}{dt} = -\frac{dJ_e^{dif}}{dz} - \frac{dJ_e^{drift}}{dz} = D_e \frac{d^2 f_e}{dz} + \mu_e \left(\mathcal{E}_z \frac{df_e}{dz} + f_e \frac{d\mathcal{E}_z}{dz} \right)$$

(132) $$\frac{df_h}{dt} = -\frac{dJ_h^{dif}}{dz} - \frac{dJ_h^{drift}}{dz} = D_h \frac{d^2 f_h}{dz} - \mu_h \left(\mathcal{E}_z \frac{df_h}{dz} + f_h \frac{d\mathcal{E}_z}{dz} \right).$$

Interacting excess charges also threaten recombination, coupling the differential equations,

(133) $$-k_{e-h} f_e f_h.$$

Equations (131) and (132) have boundary conditions defined at the electrodes. At the hole collecting electrode $z = T$ electrons are generated in the film with no possibility of collection, coupling to the exciton dissociation rate,

$$\left(-J_e^{diff} - J_e^{drift}\right)\Big|_{z=T} = \sum_i k_{dT,i} \cdot c_i(z = T). \tag{134}$$

At $z = 0$ the equivalent process occurs for holes,

$$\left(-J_h^{diff} - J_h^{drift}\right)\Big|_{z=0} = -\sum_i k_{d0,i} \cdot c_i(z = 0). \tag{135}$$

At the opposite boundary, carrier collection can be represented by a Robin boundary condition,

$$\left(-J_e^{diff} - J_e^{drift}\right)\Big|_{z=0} = k_{abs} \cdot f_e(z = 0) \tag{136}$$

$$\left(-J_h^{diff} - J_h^{drift}\right)\Big|_{z=T} = -k_{abs} \cdot f_h(z = T). \tag{137}$$

For perfect collection efficiency we have $k_{abs} \to \infty$, which we can take as arbitrarily high and check that $k_{abs} f_e(z = 0, T)$ converges.

The electric field evolves in the z axis from the gradient in excess charge populations,

$$\frac{d\mathcal{E}_z}{dz} = \frac{q}{\varepsilon}\left(f_h(z) - f_e(z)\right), \tag{138}$$

where ε is the permittivity of the film. The intrinsic bias across the film from mismatched electrode work functions,

$$\mathcal{E}_z(z = 0) = T \cdot V_{bi} \tag{139}$$

$$V_{bi} \equiv \Phi_0 - \Phi_T, \tag{140}$$

forms the boundary condition to (138), where Φ_0 and Φ_T are the work functions of materails at $z = 0$ and T respectively.

Coupled to (138), the balances (131) and (132) can be solved numerically at steady state, subject to boundary conditions (134)-(137) and (139). From the resulting carrier fluxes at $z = 0$ and $z = T$ we have the short circuit current and EQE.

Breakdown of Macroscopic Homogeneity

In our evaluation of the absorption cross-section in the light absorption problem and exciton hopping at nanotube contacts in the exciton transport problem we adopted an assumption of homogeneity at a macroscopic scale (on the order of the exciton longitudinal diffusion length). In certain reasonable film morphologies, however, there are significant variations in film density at the micron scale, even for unbundled SWNT. For example, in vacuum filtration or spin-coat deposition (Figure 5a), large voids are present. Essentially, the distribution $p(\boldsymbol{r}_c)$ is not uniform even at the macroscopic scale. The result of deviations from uniformity is that a mean film density, $\rho_{\langle l \rangle}$, is lower than the local density around a given nanotube, $\rho_{\langle l \rangle}^{loc}$. Viewed another way, the position of a given nanotube is not independent of the position of other nanotubes, but rather is correlated – a nanotube is more likely to be in some proximity to another nanotube than would be the case if their locations were independent (Figure 5b). Ideally, we would consider a radial distribution function in the plane perpendicular to the SWNT longitudinal axis, describing the probability density of another tube being at a given separation.

Above the percolation threshold density (65% close-packed density for an aligned film), the morphology of the film does not matter as conduction paths are relatively constant. This has been experimentally verified by *Maillaud et al.*[1] Below the percolation threshold, morphology plays a substantial role in film conductivity.[1]

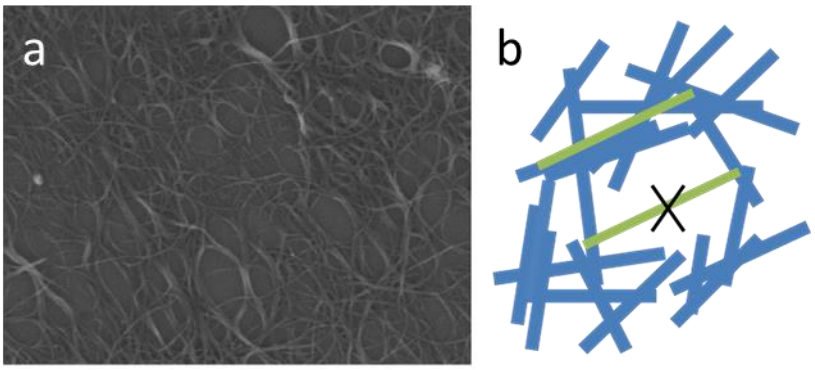

Figure 5. a) SEM image of spin-coated film of SWNT deposited from a sodium-dodecyl-sulfate solution. b) cartoon illustrating the impact of heterogeneity; a given/control nanotube (green) is not equally likely to be anywhere, but rather more likely to be close to other nanotubes.

In the light absorption problem, the effect of the error is to overestimate absorption when using a uniform $\rho_{\langle l \rangle}$; the correlation between SWNT reduces the light available at higher z in regions where SWNT is present, and no absorption occurs in voids. In the exciton transport problem, the effect of the error is to underestimate interconnect diffusivity, as the number of SWNT contacts is in reality higher. One solution to that problem is to use a SWNT-SWNT radial distribution function, $\rho(r)$, instead of a mean value of the number density, ρ, where r is the distance away from a SWNT central axis and $\rho(r)$ is the probability density that another SWNT is present at that separation. The number of contacts would then be integrated over the desired distance, rather than a fixed value,

$$\int_{d_c/2}^{d_c} \frac{1}{\frac{4}{3}\pi(2d_c)^3}\rho(r)\cdot\left(1-b_c\left(1-\frac{1}{M_B}\right)\right)\cdot l\frac{15}{4}\pi d_c^2\, dr \tag{141}$$

Fortunately, even qualitative consideration suggests that situations where this effect becomes substantial are also situations of least interest for investigation. First, high density films, within an order of magnitude of $\rho_{\langle l \rangle}^{CP}$, where this effect is minimal or nonexistent, are the films of interest for performance maximization; as we show, and has been experimentally indicated,[3] and is easy to intuit, higher density films yield higher EQE. Second, as we move towards aligned films where bundling is endemic, the exciton hopping impact of heterogeneity is mitigated.

We can also quantitatively consider the magnitude and conditions of this error. In terms of scaling, the number of interconnects increases linearly with density, and $\rho_{\langle l \rangle} < \rho_{\langle l \rangle}^{loc} < \rho_{\langle l \rangle}^{CP}$. Unless the void fraction is greater than 99%, in which case the film performance will be weak anyway, the number interconnects will be less than two orders of magnitude smaller than reality. While that seems like a large change, comparison of the diffusivities estimated puts that into perspective

$$\begin{aligned} &D_{EH,I} \to O(10^{-13}\, m^2/s) \\ &D_{EH,b} \to O(10^{-8}\, m^2/s) \\ &D_l \to O(10^{-4} m^2/s). \end{aligned} \tag{142}$$

Unless the density itself is high – in which case the void fraction is reduced – the diffusivity at interconnects plays a small role compared to any other available exciton diffusion pathway, even if bundling fractions are below 1%. In other words, the higher the void fraction, the less important SWNT interconnects become to exciton diffusion.

To relax our uniformity assumption, either simple approximations or rigorous measurement could be employed. In the former case, SEM and AFM images could be used to estimate the excess void volume in the film, and the density could be corrected where appropriate. For example, for a 30% void volume,

$$\rho_{\langle l \rangle}^{loc} \cong v^{loc}\rho_{\langle l \rangle} \tag{143}$$

$$v^{loc} = \frac{1}{1 - 0.3}.$$

More rigorously, X-Ray Diffraction (XRD) could be performed on the film to get the carbon-carbon radial distribution function. To extract the SWNT-SWNT radial distribution function from this, the intra-SWNT XRD spectrum must be either simulated or measured, and then subtracted from the film spectrum. This process is challenging and complicated.

Anisotropy of Number Density

ρ, the mean number of SWNT per volume, we employ as a defining parameter for the film. In experimental application of the present work, it is only necessary in determining $\rho_{\langle l \rangle}$, and other empirical quantities could be measured and used. In adjustments to this derivation, however, care should be taken if using ρ in any microscopic and some macroscopic scenarios for non-isotropic films. The quantity is calculated based on the total number of SWNT in the total volume. As the volume is reduced it may not scale appropriately. In a truly isotropic film, ρ can accurately describe the number of SWNT in a given volume all the way down to the point where microscopic heterogeneity arises ($O(10\ nm)$ scale). In an aligned film however, the situation depends on how the volume is shaped. Imagine a sandwiched forest of vertical SWNT. ρ is the number of SWNT divided by the total volume. If we bisect the forest vertically and consider half the volume, reducing the number of SWNT by half and the volume by half, our number density holds (Figure below). If we instead bisect it horizontally however, we cut the volume in half, but the total number of SWNT in each half hasn't changed, and our number density is grossly inaccurate. In treating SWNT interconnects we are saved because by definition the SWNT are not aligned in this case – they are essentially isotropic – and the bundled SWNT scenario relies not on ρ but rather $\rho_{\langle l \rangle}$, which *always* scales appropriately with volume. Note that $\rho_{\langle l \rangle}$ always scales appropriately with volume.

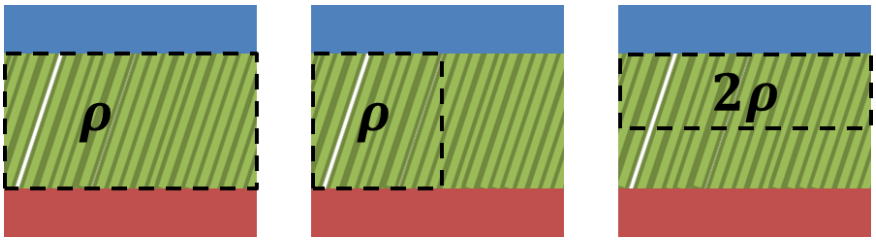

Consideration of Rayleigh Scattering and Photoluminescence

In the derivation above we opted to treat absorption as the only light-matter interaction mechanism of concern, neglecting Rayleigh scattering of light within the film and reemission from radiative decay of excitons (photoluminescence, PL). Making those assumptions has clear benefits for tractability and computation. Omitting reflection allowed us to remove $\boldsymbol{k}$ from our calculations, and omitting PL greatly simplified coupling to the exciton transport equations. The error introduced by neglecting these phenomena bears consideration however.

Fluorescence requires that an exciton radiatively decay before being quenched or diffusing to the electrodes. To achieve the latter in substantial quantities case the film must be thick, with T on the order of the radiative diffusion length, (see Results section for parameter estimates)

(144) $$L_\Gamma = \sqrt{D_l \tau_\Gamma} \cong \sqrt{10^{-2} m^2 s^{-1} \cdot 0.45 \times 10^{-9}\ s} = 2\ um.$$

As we see in the Results section, thicknesses on the order of a micron are rarely interesting. Furthermore, in the scenario when thickness is high, readsorption of the emitted light would be likely, making the net effect a dislocation of the exciton; an important phenomenon to be sure, but a second order one. To achieve a case where radiative decay could lead to a net loss of excitons, i.e. emitted light escaping, the

film would have to be thin, in which case radiative decay would be slower than separation at the electrodes. Arguments for neglecting Rayleigh scattering are similar, the losses and gains of light are, by virtue of the scattering cross-section, a higher-order consideration.

To increase the nuance and complexity of the model, fluorescence and internal reflection could still be included. In Rayleigh scattering, the photon balance (Equation (27)) should include a term transforming $\boldsymbol{k}$ appropriately. To treat the fluorescent case we would include the term

$$+k_\Gamma c(\boldsymbol{r}) \cdot \delta\left(\hbar\omega - E_{1u,i}\right) \cdot \delta\left(\boldsymbol{\epsilon} - \hat{\boldsymbol{l}}\right)$$

where $c(\boldsymbol{r})$ is excitons/volume solar cell and $k_\Gamma = 1/\tau_\Gamma$ is the radiative decay rate of excitons, and $E_{1u,i}$ is the band gap energy of chirality i. This term would couple the light absorption problem to the exciton concentration problem; given the small relative impact of fluorescence, a self-consistent method may be most efficient:

1. Solve the light absorption and exciton diffusion problems without including PL contributions to the light field.
2. Take the resulting $c(z)$, use it as an input ($\rightarrow c^{(0)}(z)$) into solving the light field problem with the fixed term
   $+k_\Gamma \cdot c^{(0)}(z) \cdot \delta\left(\hbar\omega - E_{1u,i}\right)\delta\left(\boldsymbol{\epsilon} - \hat{\boldsymbol{l}}\right)$,
   then solve the exciton concentration problem again.
3. Take that output, call it $c^{(1)}(z)$, and again plug it into the problem in the same manner.
4. Repeat the process until convergence ($c^{(n)}(z) \cong c^{(n-1)}(z)$).

Relaxing Isothermal Approximation

To relax the isothermal approximation and introduce temperature dependency to desired properties, a parallel set of ODEs solving the heat transfer problem must be coupled to our light absorption problem by the heat generated through nonradiaitve decay at the point of exciton generation, e.g.,

$$N(\boldsymbol{r}') \rightarrow N(\boldsymbol{r}', \omega) \rightarrow Q(\boldsymbol{r}') \cong \int_0^\infty N(\boldsymbol{r}', \omega) \cdot (\hbar\omega - E_0)\, d\omega \tag{145}$$

where Q is the rate of heat generation.

Including dielectric environment

The local dielectric environment has been shown to influence the size and diffusion coefficient of excitons.[11, 12] That behavior is intuitive, as it is the poor dielectric screening in two of three dimensions in a nanorod like SWNT that gives rise to the strong exciton binding energies.[12, 19-21] The impact on efficiency would be the same as adding impurities and end quenching (see Results) – it would perturb the balance between light absorption and diffusion, shifting the optimal thickness proportionally to the diffusion coefficient. Changing the dielectric would also change the absorption cross-section.[43] The present model can be made to explicitly include the local dielectric constant κ. The distribution, $p(\kappa)$, would be an additional defining property of the network, just like $p(l)$ or $\{v_i\}$. $p(\kappa)$ would include for example surfactant coverage, interstitial polymer coverage, and bundling (b_c, M_b). Relevant physical constants should then be made dependent on κ, for example $D_l \rightarrow D_l(\kappa)$.

Estimating Physical Constants

Incident Light Flux

We take the intensity and frequency distribution of incident light to be the AM1.5 solar spectrum. Even in numerical evaluation of the model, a continuous form of the spectrum is desirable for interpolation of experimental data and fine discretization of the spectrum. The spectrum can be fit to

better than 99% rms error by subtracting a series of Gaussian profiles from a geometrically attenuated blackbody spectrum. The blackbody spectrum attenuated by the atmosphere at an angle of 0.26° to the sun (angle of earth to sun) is[44]

$$b_s(E) = \frac{2F_s}{h^3c^2}\left(\frac{E^2}{e^{E/kT_s}-1}\right) \tag{146}$$

in units photons per area-time per energy photon, where $F_S = 2.16 \times 10^{-5}\,\pi$ is a geometric factor, h is Planck's constant, c is the speed of light in a vacuum, T_s is 5960K (temperature of the surface of the sun), k_B is boltzmann's constant, and E is the energy of the light. To get the flux distributed in wavelength we convert

$$b_s(\lambda = hc/E) = \frac{1}{\lambda}\cdot E \cdot b_s(E). \tag{147}$$

From the spectrum we subtract a series of Gaussian functions to fit the AM1.5 spectrum, e.g. for 60 Guassians we have

$$J_0(\lambda) \cong \frac{E}{\lambda}\cdot\frac{2F_s}{h^3c^2}\left(\frac{E^2}{e^{\frac{E}{kT_s}}-1}\right) - \sum_{i=1}^{60} A_i e^{-\frac{(\lambda-\lambda_i)^2}{2\cdot\sigma_{\lambda i}^2}}. \tag{148}$$

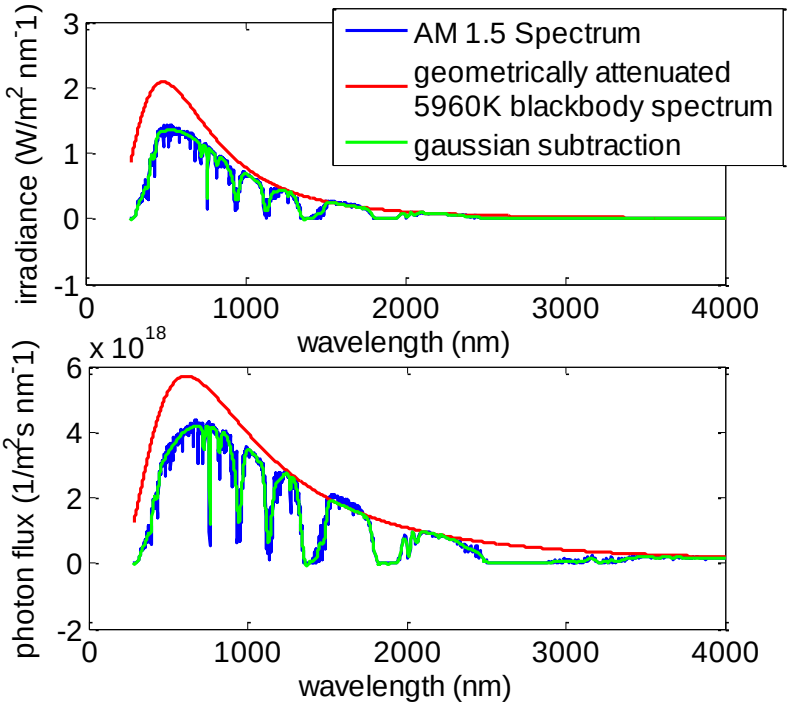

Figure 6. photon flux and irradiance distributions in wavelength for AM1.5 light, showing the experimental data (blue), 5960K blackbody spectrum attenuated by the earth-sun ray (red), and the same with 40 Gaussian curves subtracted to fit the data.

Gaussian mean (nm)	100	205.3	298.7	374.02	513.62	603.05	706.77	941.36	945.56	1052.6
Gaussian stdev (nm)	20	27.144	23.678	58.316	51.216	34.191	126.1	31.948	11.867	31.996
Gaussian maximum (W/m^2)	0.43013	6.6622	0.47979	1.2682	0.52368	0.15331	0.42537	0.29952	0.27733	0.086435
Gaussian mean	1131.7	1189.8	1314.3	1344.9	1436.9	1523	1627.7	1822	1915	2011.1

(nm)										
Gaussian stdev (nm)	20.299	23.864	24.212	43.435	56.254	23.855	72.786	33.832	46.216	9.2091
Gaussian maximum (W/m^2)	0.46103	0.091044	-0.18011	0.3014	0.23276	-0.07346	-0.01938	0.1312	0.12825	0.071032
Gaussian mean (nm)	2061	2194.6	2299	2394.2	2505.2	2600.2	2700.3	2800.1	2898.3	2999.3
Gaussian stdev (nm)	12.398	20.316	34.468	43.054	44.269	49.389	49.978	49.997	49.196	46.776
Gaussian maximum (W/m^2)	0.03767	0.003692	0.006103	0.021186	0.042016	0.036476	0.031019	0.027264	0.023936	0.017587
Gaussian mean (nm)	3100.1	3215	3305.8	3399	3500.9	3594.2	3696.5	3798.4	3899.2	3998.4
Gaussian stdev (nm)	46.272	31.193	42.886	39.739	34.614	32.971	30.404	27.578	30.045	23.088
Gaussian maximum (W/m^2)	0.020271	0.017782	0.015205	0.007778	0.004147	0.004858	0.0039	0.003244	0.004091	0.002809

Table 1. results of Guassian fit to the AM1.5 spectrum (Figure 6), where for each curve the mean, variance, and amplitude of the curve were adjusted.

(6,5) Absorption Cross-section

On resonance with the S_{22} transition the parallel polarized absorption cross-section of a single (6,5) SWNT has been measured as 3.2×10^{-17} cm^2 per carbon atom.[16] With $8.8271 \times 10^{10}\ m^{-1}$ carbon atoms per length,[16] the absorption cross-section at S_{22} per length of nanotube is

(149) $$\sigma_{l,meas}(S_{22}) = 2.92986 \times 10^{-10} \frac{m^2}{m}.$$

The wavelength dependence of $\sigma_{l,meas}(\omega)$ in general will depend on the environmental conditions, e.g., surfactant type, polymer, solid film or solution phase.[2] We estimate the dependency for a surfactant-free solid-state SWNT film by normalizing the absorbance spectrum of an isotropic film, from [2]. We scale that dependency by the S_{22} peak, at 582 nm in our data (Figure 8). Analogously to the incident solar flux, for a continuous expression we fit the data with a series of Lorentzian curves (Figure 8, Table 2)

(150) $$\sigma_{l,meas}(\lambda) \cong \sum_{i=1}^{20} \frac{A_i}{(\lambda - \lambda_i)^2 + \gamma_{\lambda i}^2}.$$

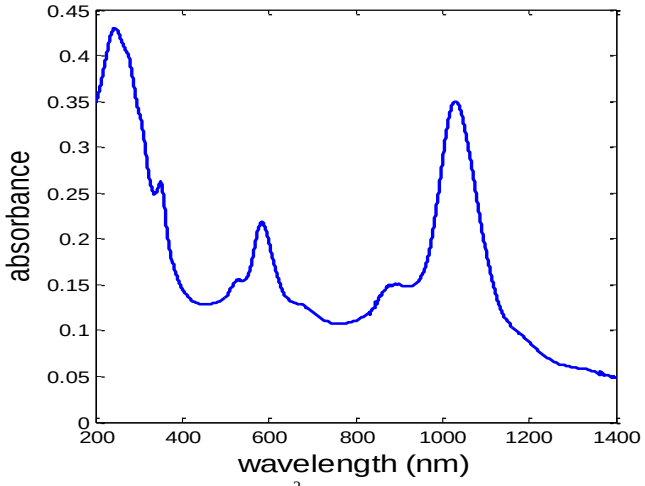

Figure 7. absorbance of isotropic film of (6,5) SWNT, from [2].

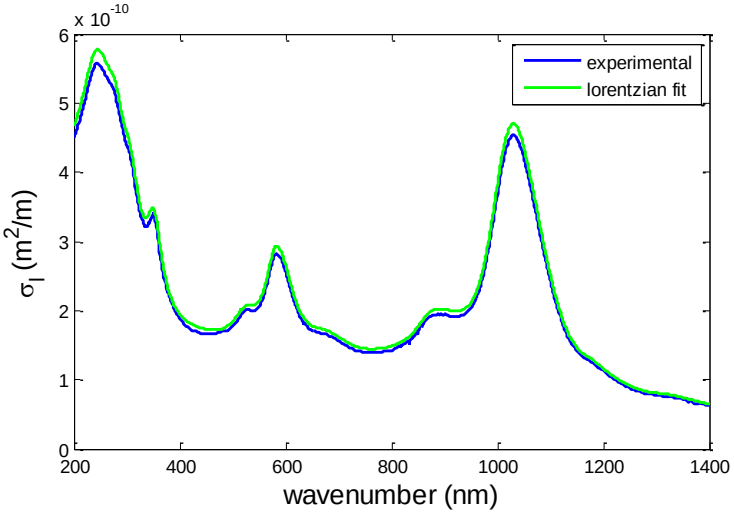

Figure 8. absorption cross-section of (6,5) SWNT as a function of wavelength, estimated from the absorbance spectrum of an isotropic surfactant-free film. For a continuous expression, data has been fit with a series of Lorentzian curves.

Mean, λ_i	$\gamma_{\lambda i}$	Amplitude, A_i ($\times 10^9$)
232.83	103.61	5000.00
242.77	19.452	22.27
308.35	12.665	7.31
278.12	27.524	69.72
352.19	13.986	18.31
489.88	89.528	408.84
524.62	21.783	17.31
579.12	22.764	42.15
594.89	35.838	127.10
676.72	54.687	130.03
788.72	200	3085.30
867.95	24.518	8.67
894.02	58.505	228.62
1005.6	32.675	86.77
1029.9	43.087	417.75
1064.2	60.168	631.40
1178.9	34.132	20.28
1216.2	57.532	62.27
1338.6	117.2	590.47
1397.7	22.647	3.18

Table 2. Fit parameter values for Lorentzian series fit of the absorption cross-section spectrum.

While the frequency dependence of $\sigma_{\parallel}(\omega)$ and $\sigma_{\perp}(\omega)$ will be different due to different optical transition modes, no polarization-dependent absorption data is available for (6,5) SWNT. We therefore crudely approximate as the same frequency dependence, and introduce the depolarization effect by an expected 1:5 net ratio of perpendicular:parallel absorbance,[45]

(151) $$\sigma_{\parallel}(\omega) = \frac{5}{6}\sigma_{l,meas}(\omega)$$

(152) $$\sigma_{\perp}(\omega) = \frac{1}{6}\sigma_{l,meas}(\omega).$$

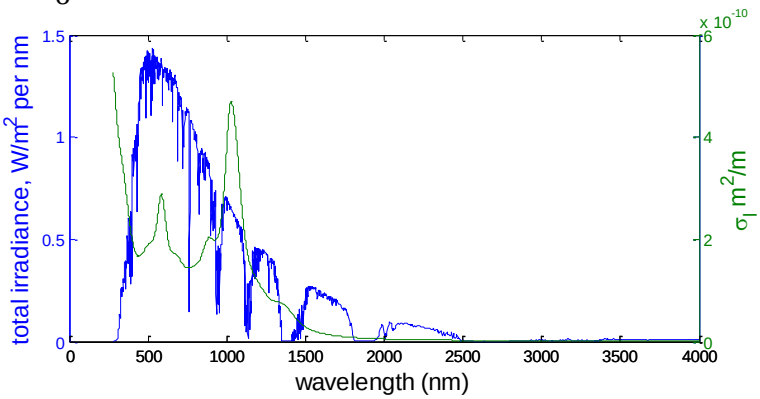

Figure 9. (6,5) isotropic absorption cross-section overlaid over solar spectrum.

Other Constants

The diameter of (6,5) SWNT is $d_{c,c-c} = 0.76\ nm$,[46] yielding an approximate $d_c = 1.095\ nm$ (see derivation above). We vary film density to investigate its influence, but benchmark values to the maximum density of a SWNT film – the close-packed density (see section below), $\rho_{\langle l \rangle}^{CP} = 9.63 \times 10^{17}\ m^{-2}$. Current fabrication methods exhibit varying densities, but at present many are far short of close-packed; vertical forests are <0.1% $\rho_{\langle l \rangle}^{CP}$,[47] and isotropic films are typically lower,[2] although horizontally aligned films have been produced up to 35% of CP density by some methods.[48, 49]

Measured values for longitudinal diffusion coefficients in SWNT span three orders of magnitude, ranging from 0.1-0.4 cm^2/s[28, 50] and 7.5-10.7 cm^2/s[36, 51] to 150-350 cm^2/s[25, 52]. Comparison of the environments of those measurements, along with comparison of other environmentally sensitive investigations,[15, 26, 27, 36, 53] strongly suggests that this variation is due to influence of the local environment on exciton-phonon scattering. Under this hypothesis, lower diffusivity values (and associated diffusion lengths) have been observed in surfactant-wrapped SWNT in solution phase, while SWNT in air exhibit the higher diffusivity values. For a solid-state film therefore we estimate $D_l \cong 100\ cm^2/s$.

For radiative decay we take a time constant of $\tau_\Gamma = 0.45\ ns$,[27, 36] yielding $k_\Gamma = 2.2 \times 10^9\ s^{-1}$. For impurity quenching, a variety of potential impurity types could be present in a film depending on the SWNT growth, separation, purification, and deposition methods; common possibilities would include lingering metal catalyst particles, sonication- or oxidation-induced sp^3 functionalization of nanotube sidewalls (lattice defect formation), and adsorbed oxygen.[30] We define some generic impurity that introduces inter-bandgap electronic states with a time constant consistent with nonradiative relaxation, $O(200\ fs)$. From that we estimate the rate constant as

(153) $$k_{im} = \sqrt{\frac{D_l}{\pi \tau_{im}}} = \sqrt{\frac{100 \times 10^{-4}}{\pi \cdot 200 \times 10^{-15}}} = 1.26 \times 10^5 \frac{m}{s}$$

and take a representative population of two generic impurities per micron of SWNT length, $n_{im} = 2 \times 10^6\ m^{-1}$ (which we vary to examine the impact of below).

The exciton-exciton annihilation rate constant we arrive at from [35] (see derivation above), with $E_{BE,(6,5)} = 0.285\ eV$ and $E_{11,(6,5)} = 1.245\ eV$,

(154) $$k_{EEA}(\boldsymbol{c}_i) = \left(6 \times 10^5 \frac{m}{s}\right)\left(\frac{E_{BE,i}}{E_i}\right)^3 \left(\frac{1.3\ eV}{0.3\ eV}\right)^3 \cong 6 \times 10^5 \frac{m}{s}.$$

End quenching we treat analogously to impurity quenching as the decay pathway is similar, giving $\tau_{end} \sim \tau_{im} \rightarrow k_{end} \cong 1.26 \times 10^5\ m/s$. Finally we estimate the exciton hopping rate constant from [3, 24] as $k_{EH} \cong 0.1\ ps^{-1} = 10^{11}\ s^{-1}$.

For free carrier physical constants, we estimate a single-SWNT free carrier mobility from [42, 54, 55] in the $10^4 - 10^5\ cm^2V^{-1}s^{-1}$ regime, taking $\mu_e^* = \mu_h^* = 5 \times 10^5\ cm^2V^{-1}s^{-1}$; under the Einstein relation (see SI) the resulting diffusivities at 300K are $D_e^* = D_h^* = 1.3\ m^2/s$. The electron-hole scattering length of $L_{eh} \cong 0.5\ um$ [55] then allows us to estimate the recombination rate constant,

(155) $$\tau_{eh} = \frac{L_{eh}^2}{D_e^*} = 1.93 \times 10^{-13}\ s$$

(156) $$k_{eh} \cong d_{6,5}^2 \sqrt{\frac{D_e^* + D_h^*}{\pi \tau_{eh}}} = 2.5 \times 10^{-12}\ m^3/s.$$

Finally we estimate the relative film permittivity as that of SWNT, ~5.

Close-packed density

The unit-cell area of hexagonally-packed SWNT, including interstitial space, is that of a rhombus with interior angle $\pi/3$ (Figure 10),

(157) $$2 \cdot d_{6,5} \cdot d_{6,5} \cdot \sin\frac{\pi}{3}\cos\frac{\pi}{3} = \frac{\sqrt{3}}{2} d_{6,5}^2.$$

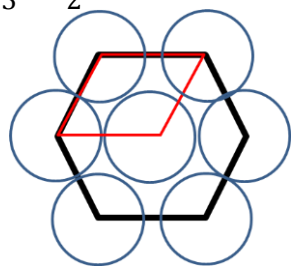

Figure 10. Cartoon of cross-section of SWNT bundle demonstrating the single-SWNT unit cell area.

This makes the length density in a bundle

(158) $$\rho_{\langle l \rangle}^{CP} = \frac{2}{\sqrt{3} d_{6,5}^2} = 9.63 \times 10^{17}\ m^{-2}.$$

Single-layer and multi-layer aligned films

As mentioned in the main text, two deposition paradigms are possible for fabrication of an aligned film. The aligned film can be grown or stacked in a single 'forest' or 'layer', which we call a single-layer (SL) film (Figure 11a). A SL film limits the possible thickness of the film, as

(159) $$T < \langle l \rangle \cos\theta'.$$

It is also possible to contact a film without end-alignment, such as in a horizontally aligned film. This is the multi-layer (ML) case (Figure 11b).

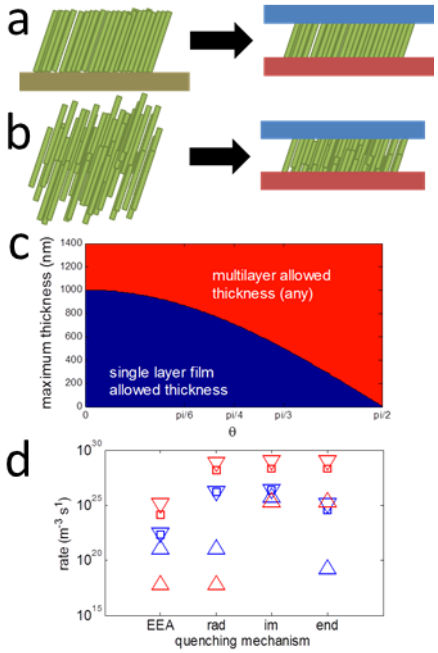

Figure 11. SL and ML film comparison. a) cartoon of a SL film, with both ends immersed in electrodes. b) cartoon of a ML film, with electrodes adhered onto a larger cake. c) allowed thickess of SL and ML films. d) comparison of quenching rates for horizontally aligned (red, $T = 200\ nm$, 80% close-packed density) and vertically aligned (blue, $T = 1\ um$), 0.3% close-packed density. End quenching is not zero in the vertically aligned (SL) case because the thickness is on the order of $\langle l \rangle$. Squares are spatially-averaged means, triangles are minima and maxima values.

A SL film will always outperform a ML film all else being equal, due to lower end quenching. In practice, SL film electrodes are likely to encompass the ends of the SWNT in the SL film, leading to

(160) $$c_{end}^{SL} = \rho^{2/3} p(l)\, cos\, \theta' \cong 0$$

where the approximation is unless the film thickness is within a standard deviation of the average SWNT length $\langle l \rangle$ (we find, however, that in optimization such thicknesses are rarely desirable). In contrast, in a ML film the end distribution is homogenous,

(161) $$c_{end} = 2\rho.$$

In the cases we examine, rather than choose between the two morphologies we often allow for both – i.e. if the film thickness is low enough for a SL film to be permissible, we use a SL film, while if it falls above that we use a ML film. In practice however the optimal film thicknesses never, except in the case of *very* low density or very low angle (e.g., horizontally aligned film), approach the limit (159).

Light absorption of aligned films

A more gradual application of the light absorption problem to aligned films is presented here, building on the *Results* section in the main paper.

Beginning our calculation with the irradiance, the absorption cross-section polarization dependence is described as equation (16) for our single chirality. We are in a position now to consider the dot product,

(162) $$\begin{aligned} \boldsymbol{\epsilon} \cdot \hat{\boldsymbol{l}} &= \epsilon_x \hat{l}_x + \epsilon_y \hat{l}_y + \epsilon_z \hat{l}_z \\ &= \sin\theta_\epsilon \cos\phi_\epsilon \sin\theta \cos\phi + \sin\theta_\epsilon \sin\phi_\epsilon \sin\theta \sin\phi \\ &\quad + \cos\theta_\epsilon \cos\theta. \end{aligned}$$

Integrating the light field balance over $p(\hat{\boldsymbol{l}})$, we have from Equation (25)

(163) $$\sigma_l(\boldsymbol{\epsilon},\omega)=\int_0^{2\pi}\int_0^{\pi}\sigma_l\left(\boldsymbol{\epsilon},\hat{\boldsymbol{l}},\omega\right)\cdot p(\theta)p(\phi)d\theta d\phi.$$

Subject to our distributions,

(164) $$p(\theta)=\delta(\theta-\theta'),\qquad \theta'\in\left[0,\frac{\pi}{2}\right],$$

(165) $$p(\phi)=\delta(\phi-0),$$

equation (163) becomes a sifting integral yielding $\theta=\theta'$ and $\phi=0$. Our absorption cross-section becomes,

(166) $$\sigma_l(\boldsymbol{\epsilon},\omega)=\sigma_{l,meas}(\omega)\left(\frac{5}{6}(\sin\theta_\epsilon\cos\phi_\epsilon\sin\theta'+\cos\theta_\epsilon\cos\theta')^2+\frac{1}{6}(1-|\sin\theta_\epsilon\cos\phi_\epsilon\sin\theta'-\cos\theta_\epsilon\cos\theta'|)^2\right).$$

Solving the photon balance (34) with no z dependence to $\rho_{\langle l\rangle}$ or σ_l, subject to the incident unpolarized solar flux boundary condition (36), our forward flux becomes

(167) $$J_F(\omega,\boldsymbol{\epsilon}|z)=J_0(\omega)\cdot\delta\left(\theta_\epsilon-\frac{\pi}{2}\right)\cdot\frac{1}{2\pi}\cdot\exp\left[-\rho_{\langle l\rangle}\sigma_{l,meas}(\omega)\left(\frac{5}{6}(\sin\theta_\epsilon\cos\phi_\epsilon\sin\theta'+\cos\theta_\epsilon\cos\theta')^2+\frac{1}{6}(1-|\sin\theta_\epsilon\cos\phi_\epsilon\sin\theta'-\cos\theta_\epsilon\cos\theta'|)^2\right)\cdot z\right].$$

Integrating over θ_ϵ is trivial with the sifting property of $\delta(\cdot)$, yielding

(168) $$J_F(\omega,\phi_\epsilon|z)=\frac{1}{2\pi}J_0(\omega)\cdot\exp\left[-\rho_{\langle l\rangle}\sigma_{l,meas}(\omega)\left(\frac{5}{6}(\cos\phi_\epsilon\sin\theta')^2+\frac{1}{6}(1-|\cos\phi_\epsilon\sin\theta'|)^2\right)z\right].$$

Note that except in the vertically-aligned case ($\theta'=0$), there is a polarization dependence to the field absorption. We can integrate over all frequencies to get the flux gradient at each polarization, or integrate over all polarization angles to get the flux gradient at each frequency.

With a boundary condition of reflectance R off the back electrode we solve the reverse flux differential equation, again substituting in $\sigma_l(\boldsymbol{\epsilon},\omega)$ and integrating over θ_ϵ to yield

(169) $$J_R(\omega,\phi_\epsilon|z)=\frac{1}{2\pi}\cdot R\cdot J_0(\omega)\cdot\exp\left[-\rho_{\langle l\rangle}\sigma_{l,meas}(\omega)\left(\frac{5}{6}(\cos\phi_\epsilon\sin\theta')^2+\frac{1}{6}(1-|\cos\phi_\epsilon\sin\theta'|)^2\right)\cdot(2T-z)\right].$$

The total light field gradient would then be

(170) $$J_\nu(\omega,\phi_\epsilon|z)=J_R(\omega,\phi_\epsilon|z)+J_F(\omega,\phi_\epsilon|z),$$

for example plotted in Figure 3 of the main paper for horizontally and vertically aligned films.

Supplemental information for aligned film results

In addition to the results presented in the main text, a variety of other figures are relevant. In Figure 12 we can look at the exciton concentration in the horizontally and vertically aligned films presented in the main paper, noting the low (<10 nm) diffusion length of the horizontally-aligned film. We can also look at the relative rates of each quenching mechanism considered, observing that exciton-exciton auger annihilation plays a minor role in device performance.

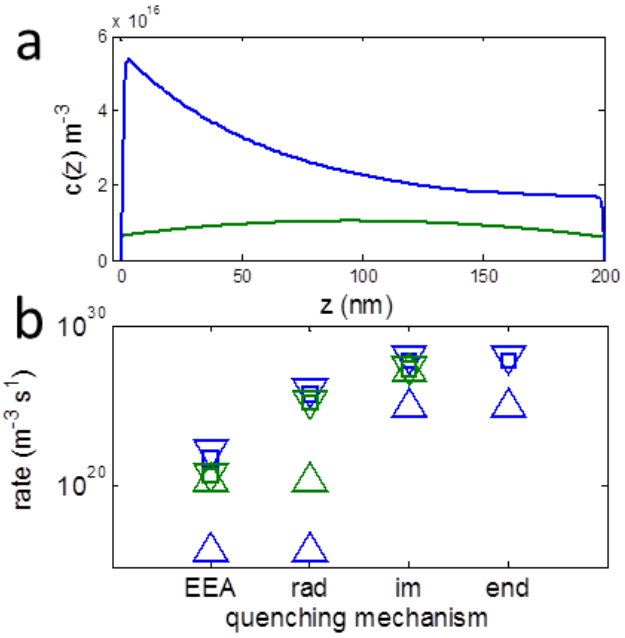

Figure 12 Comparison of exciton transport behavior in vertically (green) and horizontally (blue) aligned films at $T = 40\,nm$, $\rho_{\langle l \rangle} = 0.8\rho^{CP}_{\langle l \rangle}$, $R = 1$. a) exciton concentration at depth z in the film. Note the short (<10 nm) diffusion length of excitons in the horizontally-aligned film, leading to poor collection even at high concentrations. b) mean (squares) and minimum/maximum (triangles) quenching rates for each mechanism of interest. Note log scale.

We can observe a few interesting features of varying the mean length of nanotubes in the network. By condensing the 2D maps in the main paper in 1D plots of efficiency versus thickness at varying density, we can easily visualize the shift in optimal thicknesss T^* as density rises (Figure 13).

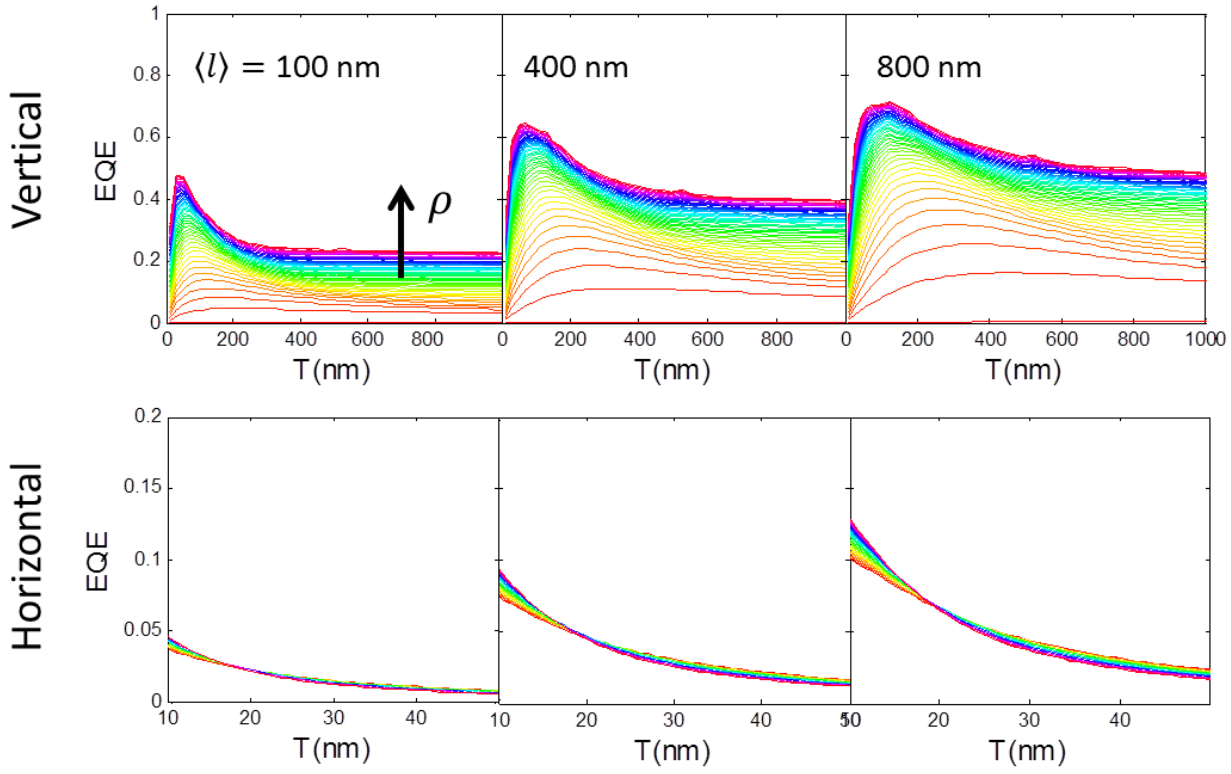

Figure 13. Performance versus thickness curves with increasing density for vertically and horizontally aligned films. These plots are the same data as the 2D maps presented in the main paper, but visualized as a series of 1D curves. Black arrow indicates the direction of increasing density (red to blue to purple). In the vertically aligned case the shift of the optimal thickness downward is clear, particularly the asymptote to $T^* \to \infty$ as $\rho \to 0$.

In Figure 14 we look at the trend of EQE with $\langle l \rangle$ for vertically and horizontally aligned films, and different thicknesses and densities. In all cases we find that performance monotonically increases with nanotube length, as we would intuit given that end-quenching is a purely undesirably phenomenon, but that there are diminishing returns with increasing length – again as we would intuit – leading to an asymptote as $\langle l \rangle \to \infty$, where performance is limited by the balance of light absorption and the thickness of the film.

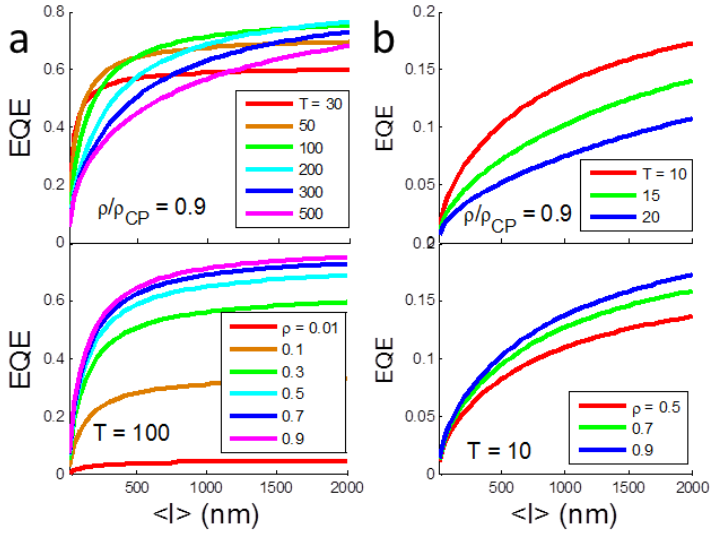

Figure 14. Trends of performance with mean length for vertically (a) and horizontally (b) aligned films. Top charts compare trends at different thicknesses and 0.9 CP density. Bottom charts compare trends at different densities and 100 nm thickness.

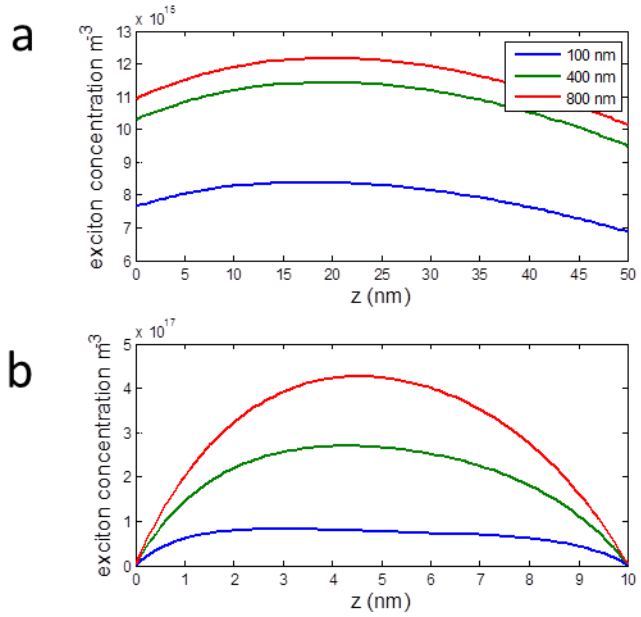

Figure 15. Exciton concentration gradients in vertically (a) and horizontally (b) aligned films with different mean lengths and 30% CP density.

We noted in the main paper the compelling match of a power law trend to the optimal thickness versus density. For vertically aligned films, we can plot more curves and extract trends of the coefficients to validate the results against more data. Numerical results exhibit noise because of low sensitivity ($O(10\ nm)$) of EQE to thickness close to the optimum.

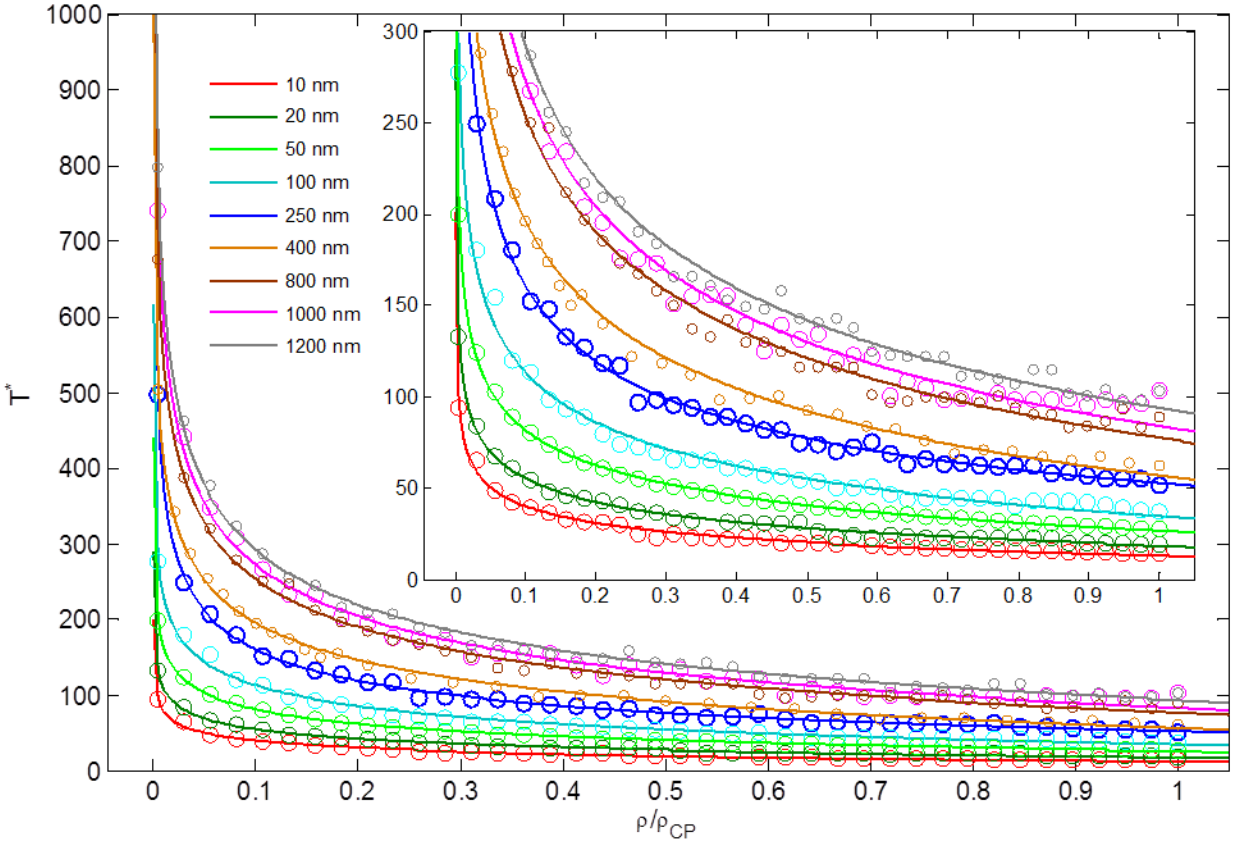

Figure 16. Trend of optimal thickness T^* with density at different mean lengths $\langle l \rangle$. Open circles are numerical optimization results, and curves are power law fits $T^* = a\left(\frac{\rho}{\rho_{CP}}\right)^b + c$.

Table 3. Power and biexponential fits of trends in optimal thickness with density, at different mean lengths. Note that error in the power law trend is entirely within optimization limits, which are $\pm O(10)\ nm$. Trends in power law a, b, c parameters are in the SI.

Power law description of optimal thickness trend

	Power Fit $\left(T^* = a\left(\frac{\rho}{\rho_{CP}}\right)^b + c\right)$					Biexponential Fit	
Nanotube Length $\langle l \rangle$	a (nm)	b $\left(\frac{\rho}{\rho_{CP}}\right)^{-1}$	c (nm)	R^2	rms error (nm)	R^2	rms error (nm)
10 nm	56	-0.172	-42.6	0.992	1.5		
20 nm	68	-0.187	-50	0.996	1.5		
50 nm	101	-0.189	-75	0.999	1.0	0.992	3.1
100 nm	148	-0.186	-113	0.992	4.2		

400 nm	230	-0.205	-174	0.998	3.6	0.990	8.6
800 nm	254	-0.229	-176	0.997	6.5	0.987	13.2
1000 nm	248	-0.246	-166	0.995	9.0		
1200 nm	245	-0.255	-155	0.997	6.8	0.989	13.7

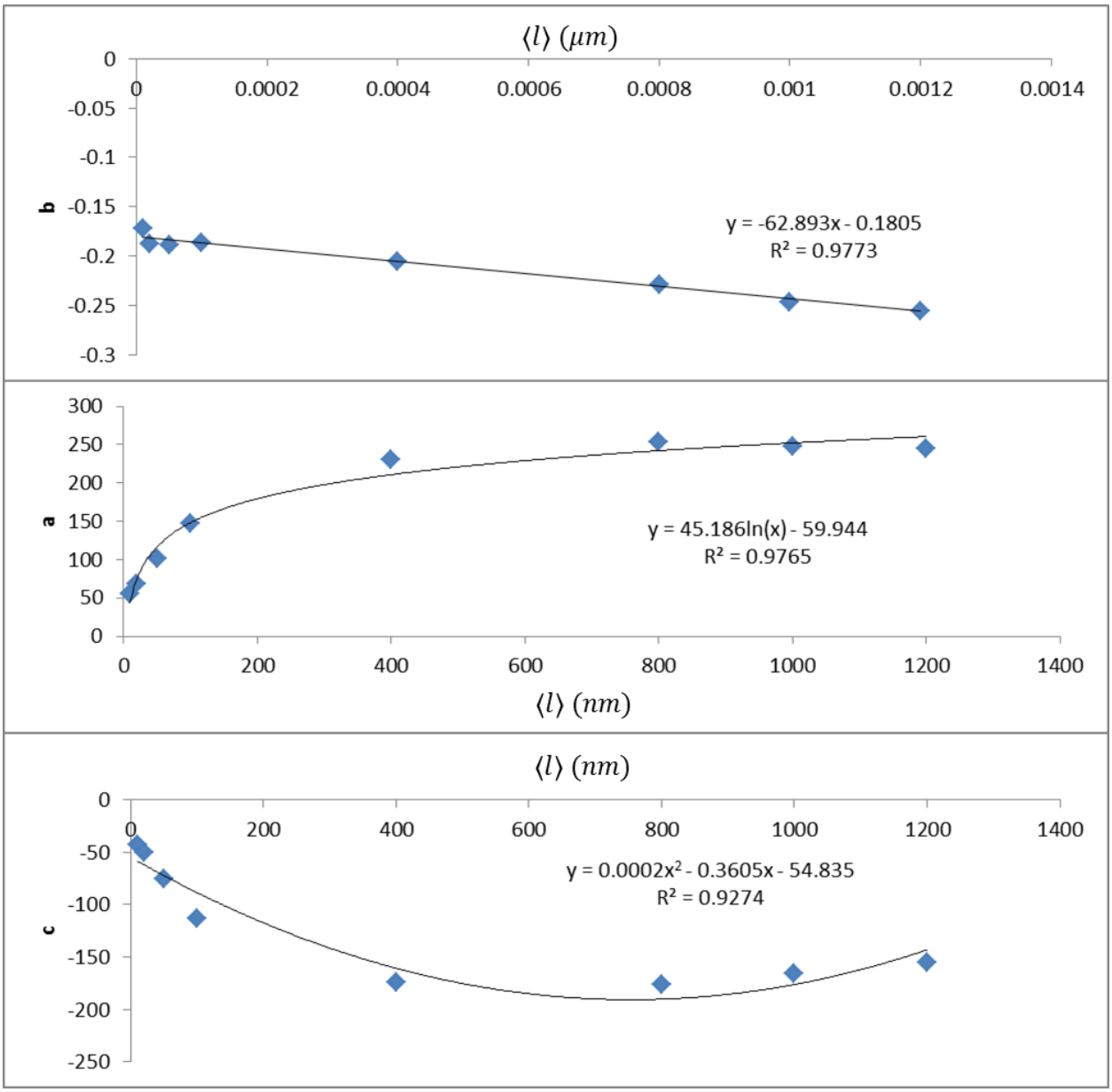

Figure 17. Trends of power law coefficients, a, b, c, with mean length $\langle l \rangle$. While the linear fit of the power coefficient (b) is compelling, logarithmic and quadratic fits for the proportionality factor (a) and intercept (c) are not entirely convincing. We find that the relationship of a and c however *does* follow a power trend, see main paper. See main paper for data table.

In the main paper, a trend of T_{CP}^* with $\langle l \rangle$ is observed, reproduced here in Figure 18. We can evaluate the quality of the trend rigorously to conclude that it is a perfect fit: the slope 95% confidence interval, 0.0212, is 1/100th of the equivalent error in T_{CP}^* resulting from numerical optimization methods.

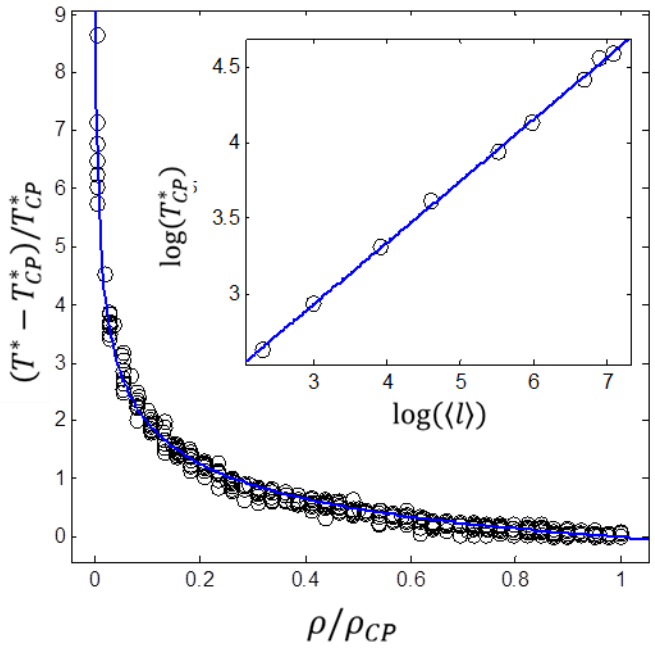

Figure 18. (copied from main text) Trend of optimal thickness numerical results with density, plotted relative to optimal thickness at close-packed density (see text). The data (black circles) includes results from devices with $\langle l \rangle = 10, 20, 50, 100, 250, 400, 800, 1000,$ and $1200\ nm$, showing that on this plot they all collapse to a single trend. The blue curve is a fit of equation (39) in the main paper, showing perfect agreement (well within numerical result variation). The inset show the trend of the optimal thickness at close-packed density (T^*_{CP}) with mean nanotube length (inverse impurity concentration) on a log-log scale, showing that they exhibt a strict power law relationship.

We also can for interest take cross-sections of the orientation-thickness maps along a thickness, 200 nm, at different densities to see the emergence of an intermediate angle.

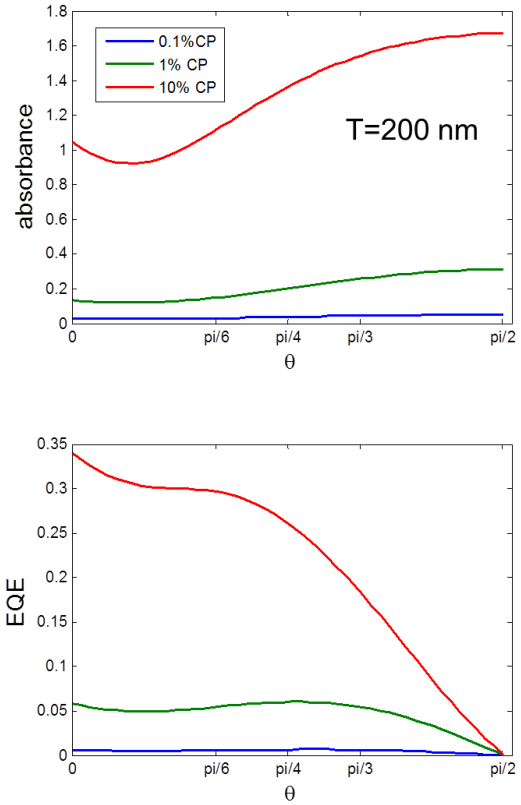

Figure 19. absorbance and efficiency curves with alignment angle for devices 200 nm thick. $\langle l \rangle = 400\ nm, n_{im} = 2e6\ m^{-1}, R = 1$.

Isotropic Case

The second case we consider is an isotropic film, where SWNT orientation in any axis is equally likely,

(171) $$p(\theta) = \frac{1}{\pi}, \qquad \theta \in [0, \pi]$$

(172) $$p(\phi) = \frac{1}{2\pi}, \qquad \phi \in [0,2\pi].$$

This system differs from current 'isotropic' experimental systems in that those systems in practice restrict θ, making them more of a 'sandwich' architecture and more similar to off-horizontal aligned films. Even when caste with surfactant we expect some level of bundling to be typical in an isotropic network, and take a baseline for comparison of $b_c = 0.1$, $M_b = 4$.

Our treatment of the light field is analogous to the aligned case application, but the integral over $p(\hat{\boldsymbol{l}})$ becomes less trivial,

(173) $$\sigma_l(\boldsymbol{\epsilon}, \omega) = \frac{1}{\pi}\frac{1}{2\pi}\frac{1}{6}\sigma_{l,meas}(\omega)\int_0^{2\pi}\int_0^{\pi} 5{\varepsilon_\parallel}^2 + \left(1 - \left|\varepsilon_\parallel\right|\right)^2 d\theta d\phi.$$

(25) is solvent, and yields (see section below, moved for brevity)

(174) $$\sigma_l(\boldsymbol{\epsilon}, \omega) = \left(\frac{5}{12} - \frac{4}{3\pi^2}\right)\sigma_{l,meas}(\omega).$$

Note that we no longer have any ϕ_ϵ dependence to absorption, as we would intuit from an isotropic distribution. Our light field becomes

(175) $$J_F(\omega|z) = J_0(\omega) \cdot \exp\left[-\left(\frac{5}{12} - \frac{4}{3\pi^2}\right)\rho_{\langle l\rangle}\sigma_{l,meas}(\omega) \cdot z\right].$$

(176) $$J_R(\omega|z) = R \cdot J_0(\omega) \cdot \exp\left[-\left(\frac{5}{12} - \frac{4}{3\pi^2}\right)\rho_{\langle l\rangle}\sigma_{l,meas}(\omega) \cdot (2T - z)\right].$$

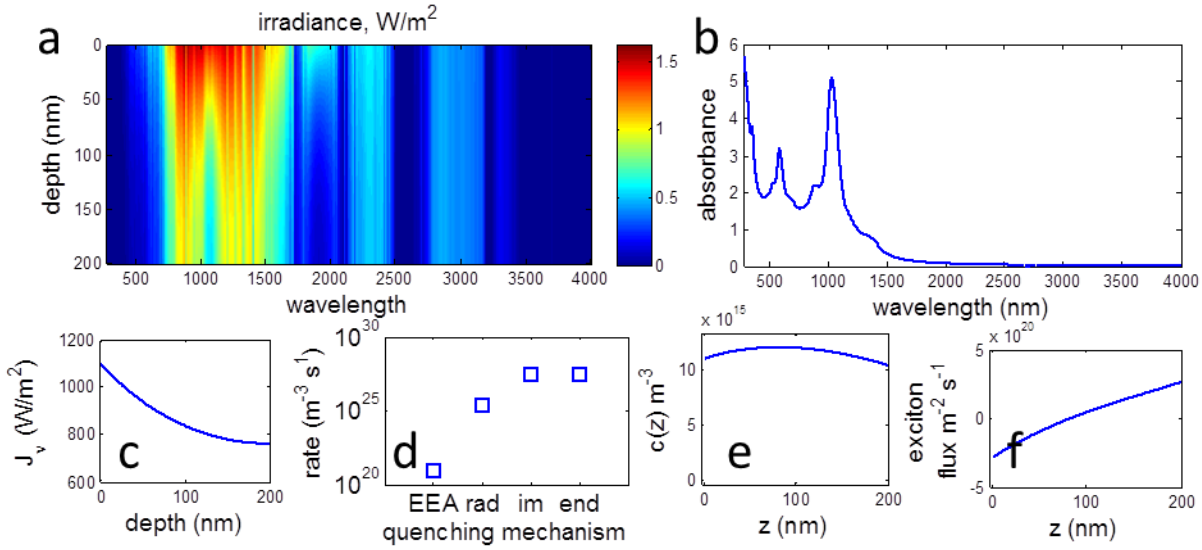

Figure 20. Light field attenuation and steady-state exciton transport for an isotropic monochiral (6,5) film with $T = 200\,nm$, $R = 1$, $\rho_{\langle l\rangle} = 0.1\rho^{CP}_{\langle l\rangle}$, $b_c = 0.1$, and $M_b = 4$. a) irradiance gradient as a function of wavelength. Note stronger attenuation on resonance. b) total film absorbance as a function of wavelength. c) total irradiance as a function of depth in the field. d) mean quenching rates by each mechanism. Note log scale. e) exciton concentration gradient. f) exciton flux through the depth of the film.

Moving on to the exciton concentration gradient, our expressions are the same as in the aligned film case, with the end concentration being $c_{end} = 2\rho$. Integrating the monochiral exciton balance (101) over orientation distribution $p(\theta)$ we get the diffusion coefficient,

(177) $$D_{tot} = \frac{1}{\pi}\int_0^{\pi} D_l(\cos\theta)^2 + (1 - |\cos\theta|)^2\left(\gamma_I D_{EH,I} + b_c D_{EH,b}\right) d\theta$$

which resolves to

(178) $$D_{tot} = \frac{1}{2\pi}\left(\pi D_l + (3\pi - 8)\left(\gamma_I D_{EH,I} + b_c D_{EH,b}\right)\right).$$

D_l, $D_{EH,I}$, $D_{EH,b}$, and γ_I follow as their definitions, with the mean squared coalignment becoming (see Derivation)

(179) $$\langle\lambda^2\rangle = \frac{1}{4}\frac{1}{\pi^4} \cdot \frac{9\pi^4}{64} = \frac{9}{256}.$$

Beyond examining particular cases (Figure 20), we can proceed to explore the parameter space, particularly the thickness-density relation (Figure 21). Again we see a strong optimum T^* emerge as a function of density. As density rises, the enhanced absorbance makes lower thicknesses with shorter generated exciton-electrode separations preferable. Again we see a large improvement in performance with density at low density; higher density improves absorbance, increases inter-SWNT hopping, and reduces (at fixed concentration) exciton-exciton annihilation and end-quenching. In general we note similar performance trends compared to aligned films with modest vertical components.

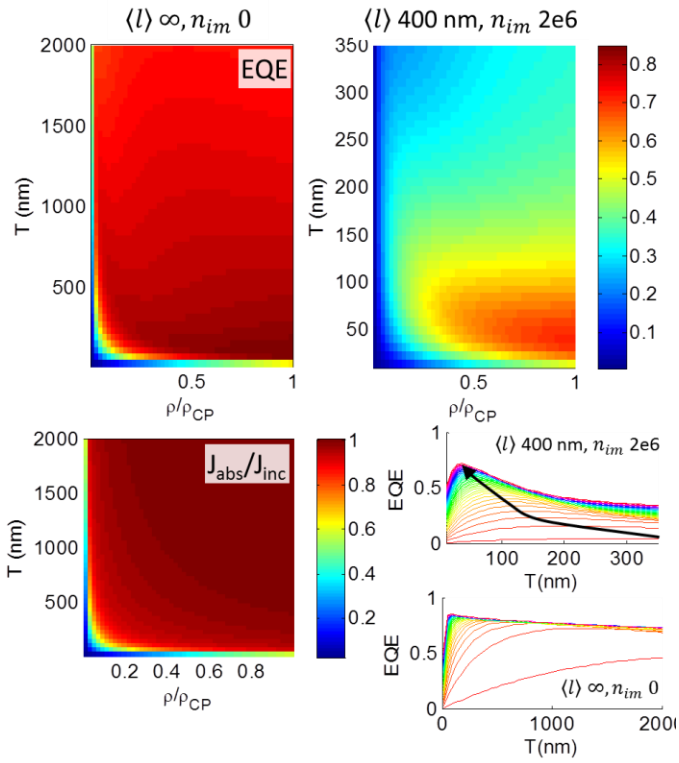

Figure 21. Density-thickness optimization of isotropic films, with = 1, $b_c = 0.1$, and $M_b = 4$. a) performance for 'idealized' film. b) fraction of light absorbed. c) performance for film with $\langle l \rangle = 400\ nm$, 2 impurities per micron. d) performance versus T plots at each density sampled in (a) and (c), the arrow indicates path of T^* in (c).

Isotropic absorption cross-section

For brevity, resolution of the integral

$$\sigma_l(\boldsymbol{\epsilon}, \omega) = \frac{1}{\pi}\frac{1}{2\pi}\frac{1}{6}\sigma_{l,meas}(\omega)\int_0^{2\pi}\int_0^{\pi} 5{\varepsilon_\parallel}^2 + \left(1 - \left|\varepsilon_\parallel\right|\right)^2 d\theta d\phi, \tag{180}$$

$$\varepsilon_\parallel = \boldsymbol{\epsilon}\cdot\hat{\boldsymbol{l}} = \sin\theta_\epsilon\cos\phi_\epsilon\sin\theta\cos\phi + \sin\theta_\epsilon\sin\phi_\epsilon\sin\theta\sin\phi + \cos\theta_\epsilon\cos\theta, \tag{181}$$

is omitted from the section above; we pursue it here. First, we recognize that when we integrate over θ_ϵ the incident light $\delta(\cdot)$ function will sift to $\theta_\epsilon = \frac{\pi}{2}$, simplifying

$$\varepsilon_\parallel \to \cos\phi_\epsilon\sin\theta\cos\phi + \sin\phi_\epsilon\sin\theta\sin\phi. \tag{182}$$

Next, we note the identity

$$(1 - |x|)^2 = |x|^2 + 1 - 2|x| = x^2 + 1 - 2|x|. \tag{183}$$

Applying this our integral simplifies to

$$6\int_0^{2\pi}\int_0^{\pi}{\varepsilon_\parallel}^2 d\theta d\phi + \int_0^{2\pi}\int_0^{\pi} d\theta d\phi - 2\int_0^{2\pi}\int_0^{\pi}\left|\varepsilon_\parallel\right| d\theta d\phi \tag{184}$$

which further simplifies with

$$\int_0^{2\pi}\int_0^{\pi}{\varepsilon_\parallel}^2 d\theta d\phi = \frac{1}{2}\pi^2 \tag{185}$$

giving us

$$\sigma_l(\boldsymbol{\epsilon},\omega) = \frac{1}{\pi}\frac{1}{2\pi}\frac{1}{6}\sigma_{l,meas}(\omega)\left(3\pi^2 + 2\pi^2 - 2\int_0^{2\pi}\int_0^{\pi}\left|\varepsilon_{\parallel}\right|\, d\theta d\phi\right). \tag{186}$$

We then approach the absolute value integral. $\cos\theta$ is always positive over the domain, allowing us to easily evaluate the inner integral,

$$\begin{aligned}\int_0^{2\pi}\int_0^{\pi}\left|\varepsilon_{\parallel}\right|\, d\theta d\phi &= 2\int_0^{2\pi}\left|\sin(\phi)\sin(\phi_\epsilon) + \cos(\phi)\cos(\phi_\epsilon)\right| d\phi \\ &= 2\int_0^{2\pi}\left|\cos(\phi-\phi_\epsilon)\right| d\phi.\end{aligned} \tag{187}$$

Fortuitously, the remaining integral splits over four domains with definite sign regardless of the value of ϕ_ϵ,

$$2\int_0^{2\pi}\left|\cos(\phi-\phi_\epsilon)\right| d\phi = 8. \tag{188}$$

Our expression is then resolved,

$$\sigma_l(\boldsymbol{\epsilon},\omega) = \left(\frac{5}{12} - \frac{4}{3\pi^2}\right)\sigma_{l,meas}(\omega). \tag{189}$$

Table of Variables

In order of introduction.

x, y, z	Cartesian coordinates. The z axis is perpendicular to the plane heterojunction. $z = 0$ is in the top of the film.
J_0	Incident solar flux, AM1.5 light. Unpolarized in the xy plane, incident in z^+.
T	SWNT film thickness.
R	Back electrode reflectance.
l	Length of a single nanotube
$\hat{l} = (\theta, \phi)$	Orientation, in spherical coordinates, of a single nanotube.
$\boldsymbol{l} \equiv (l, \theta, \phi)$	Length and orientation vector of a nanotube (the vector along its central axis).
$\boldsymbol{r}_c$	Vector to/position of the center of a single nanotube in the film.
$\boldsymbol{r}'$	Vector to/position of particular points along the central axis of a nanotube in the film, in Cartesian dimensions.
α_l	Fraction along the length of the nanotube describing a position along the tube.
r_l	One-dimensional coordinate along the length of a nanotube.
$\boldsymbol{c}_i$	Chirality of a nanotube, (n_1, n_2), indexed arbitrarily by integer $i \in \mathbb{Z}$, defining $E_{i+1} > E_i$.
$d_{\boldsymbol{c},c-c}$	Center-to-center diameter of a nanotube of chirality $\boldsymbol{c}$, i.e. from the center of one wall to the center of the other.
$d_{\boldsymbol{c}}$	Effective outer diameter of a carbon nanotube of chirality $\boldsymbol{c}$.
a_0	Graphene lattice constant
v_i	Fraction of chirality i represented in the film, by number density.
$J_v(\boldsymbol{r})$	Total photon flux at position $\boldsymbol{r}$, across all wavelengths, polarizations, and propagation directions.
ω	Frequency.
$\boldsymbol{\epsilon} \equiv (\theta_\epsilon, \phi_\epsilon)$	Linear polarization angle of irradiance, in spherical coordinates.
$\boldsymbol{k} \equiv (\theta_k, \phi_k)$	Propagation direction of irradiance, in spherical coordinates.
$\sigma(\boldsymbol{c}, \boldsymbol{\epsilon}, \hat{\boldsymbol{l}}, \omega)$	Absorption cross-section of a nanotube per atom or mole of carbon.

$\boldsymbol{\mu}_{\parallel}(\boldsymbol{c},\omega)$, $\boldsymbol{\mu}_{\perp}(\boldsymbol{c},\omega)$	Parallel (longitudinal) and perpendicular (axial) transition dipoles of a carbon nanotube, representing optically-active electronic transitions between electronic states with periodicity in those orientations.
$\sigma_l(\boldsymbol{c},\boldsymbol{\epsilon},\hat{\boldsymbol{l}},\omega)$	Absorption cross-section of a carbon nanotube per length of carbon nanotube.
$\sigma_{l,meas},\sigma_{\parallel},\sigma_{\perp}$	Empirically-measured absorption cross-sections of carbon nanotubes per length of carbon nanotube.
ρ	Number density of carbon nanotubes in the network (number of nanotubes per volume). See SI section for discussion of spatial variation.
$\rho_{\langle l\rangle}$	Length of carbon nanotubes per volume of film. See SI section for heterogeneity issues.
$N_i(\boldsymbol{r})$	Photon absorption rate due to chirality i.
$N(\boldsymbol{r})$	Photon absorption rate.
$N_p(\boldsymbol{r})$	Photon 'concentration' at position $\boldsymbol{r}$.
t	Time
J_F, J_R	Forward and reverse photon fluxes.
D_l	Diffusion coefficient in one dimension along a nanotube, i.e. the longitudinal diffusion coefficient.
E_i	First optical (exciton) band gap of chirality i (see text). It is the single-photon active transition (ground state → 1u), alternatively labeled $E_{1u,i}$, or E_{1u} when ignoring the chiral index.
ω_{1u}	Frequency of light resonant with ground state to 1u electron transition, i.e. $\omega_{1u} = E_{1u}/\hbar$.
$E_{0,i}$	Ground state electron energy, in chirality i.
$n(r_l)$	One-dimensional exciton concentration along the length of a nanotube.
$c(\boldsymbol{r})$	Exciton concentration at position $\boldsymbol{r}$.
$k_\Gamma = 1/\tau_\Gamma$	Radiative decay constant and radiative decay constant.
k_{im}	Quenching rate constant from local impurities.
n_{im}	Concentration of local impurities along carbon nanotubes.
k_{EEA}	Exciton-exciton auger recombination rate constant.
$E_{BE,i}$	Exciton binding energy for chirality i.
k_{end}	End-quenching rate constant.
$c_{end}(\boldsymbol{r})$	Concentration of nanotube ends.
$\Delta, \Delta_I, \Delta_B$	Separation between center of two nantoubes, at interconnects (I) and bundles (B).
k_{EH}	Exciton hopping rate between nanotubes.
λ	Co-alignment of two nanotubes.
$D_{EH}, D_{EH,b}, D_{EH,I}$	Orthogonal (inter-SWNT) diffusion coeffient, at bundles and interconnects.
χ	Number of nearest neighbors around a nanotube in a bundle.
M_B	Mean bundle size (in number of nanotubes)
b_c	Fraction of bundles in the film, in length of nanotubes in bundles per total length of nanotubes.
γ_I	Defined constant that could be understood as the 'sparsity'.
A_I	Interstitial modifier – the fraction of the surface of nanotubes that are covered in a material such that they block inter-SWNT contacts.
D_{tot}	Total film diffusion coefficient in the z axis.
v_m	Fraction of mSWNT in the film
D_e, D_h	Electron and hole free carrier diffusion coefficients.
μ_e, μ_h	Electron and hole free carrier mobilities.
k_B	Boltzmann constant
q	Elementary charge
f_e, f_h	Free carrier concentrations

J_e, J_h	Free carrier fluxes
k_{e-h}	Electron-hole recombination rate constant
$\mathcal{E}_z$	Electric field
ε	Mean dialectric constant of film
V_{bi}	Intrinsic bias across the film due to work function offset.

References

1. Maillaud, L.; Zakri, C.; Ly, I.; Pénicaud, A.; Poulin, P., Conductivity of transparent electrodes made from interacting nanotubes. *Applied Physics Letters* **2013,** *103* (26), -.
2. Jain, R. M.; Howden, R.; Tvrdy, K.; Shimizu, S.; Hilmer, A. J.; McNicholas, T. P.; Gleason, K. K.; Strano, M. S., Polymer-Free Near-Infrared Photovoltaics with Single Chirality (6,5) Semiconducting Carbon Nanotube Active Layers. *Adv Mater* **2012,** *24* (32), 4436-4439.
3. Bindl, D. J.; Shea, M. J.; Arnold, M. S., Enhancing extraction of photogenerated excitons from semiconducting carbon nanotube films as photocurrent. *Chem Phys* **2013,** *413*, 29-34.
4. Bernardi, M.; Lohrman, J.; Kumar, P. V.; Kirkeminde, A.; Ferralis, N.; Grossman, J. C.; Ren, S. Q., Nanocarbon-Based Photovoltaics. *Acs Nano* **2012,** *6* (10), 8896-8903.
5. Reich, S.; Thomsen, C.; Maultzsch, J., *Carbon nanotubes : basic concepts and physical properties*. Wiley-VCH: Weinheim ; Cambridge, 2004; p ix, 215 p.
6. Ni, Z. H.; Wang, H. M.; Kasim, J.; Fan, H. M.; Yu, T.; Wu, Y. H.; Feng, Y. P.; Shen, Z. X., Graphene Thickness Determination Using Reflection and Contrast Spectroscopy. *Nano Lett* **2007,** *7* (9), 2758-2763.
7. Usual convention is to bundle the direction of propagation and the frequency of the electric field, i.e. k=2π/ω, to be consistent with the plane wave representation of light. Since we will not exploit the plane wave character of light here however it becomes, for reasons clear later, more convenient to separate the frequency of light from the orientation of it, thus k is an orientation vector only, it does not connect with the spatial variation of the electric field.
8. Naumov, A. V.; Tsyboulski, D. A.; Bachilo, S. M.; Weisman, R. B., Length-dependent optical properties of single-walled carbon nanotube samples. *Chem Phys* (0).
9. Cherukuri, T. K.; Tsyboulski, D. A.; Weisman, R. B., Length- and Defect-Dependent Fluorescence Efficiencies of Individual Single-Walled Carbon Nanotubes. *Acs Nano* **2012,** *6* (1), 843-850.
10. Hagen, A.; Hertel, T., Quantitative Analysis of Optical Spectra from Individual Single-Wall Carbon Nanotubes. *Nano Lett* **2003,** *3* (3), 383-388.
11. Perebeinos, V.; Avouris, P., Exciton ionization, Franz-Keldysh, and stark effects in carbon nanotubes. *Nano Lett* **2007,** *7* (3), 609-613.
12. Avouris, P.; Freitag, M.; Perebeinos, V., Carbon-nanotube photonics and optoelectronics. *Nat Photonics* **2008,** *2* (6), 341-350.
13. Schoppler, F.; Mann, C.; Hain, T. C.; Neubauer, F. M.; Privitera, G.; Bonaccorso, F.; Chu, D. P.; Ferrari, A. C.; Hertel, T., Molar Extinction Coefficient of Single-Wall Carbon Nanotubes. *J Phys Chem C* **2011,** *115* (30), 14682-14686.
14. Barkelid, M.; Steele, G. A.; Zwiller, V., Probing Optical Transitions in Individual Carbon Nanotubes Using Polarized Photocurrent Spectroscopy. *Nano Lett* **2012,** *12* (11), 5649-5653.
15. Xiao, Y. F.; Nhan, T. Q.; Wilson, M. W. B.; Fraser, J. M., Saturation of the Photoluminescence at Few-Exciton Levels in a Single-Walled Carbon Nanotube under Ultrafast Excitation. *Phys Rev Lett* **2010,** *104* (1).
16. Oudjedi, L.; Parra-Vasquez, A. N. G.; Godin, A. G.; Cognet, L.; Lounis, B., Metrological Investigation of the (6,5) Carbon Nanotube Absorption Cross Section. *The Journal of Physical Chemistry Letters* **2013,** *4* (9), 1460-1464.

17. Fitzpatrick, R. Approximation Methods. http://farside.ph.utexas.edu/teaching/qm/lectures/node48.html.
18. Wang, N.; Tang, Z. K.; Li, G. D.; Chen, J. S., Materials science: Single-walled 4 A carbon nanotube arrays. *Nature* **2000,** *408* (6808), 50-51.
19. Wang, F.; Dukovic, G.; Brus, L. E.; Heinz, T. F., The optical resonances in carbon nanotubes arise from excitons. *Science* **2005,** *308* (5723), 838-841.
20. Maultzsch, J.; Pomraenke, R.; Reich, S.; Chang, E.; Prezzi, D.; Ruini, A.; Molinari, E.; Strano, M. S.; Thomsen, C.; Lienau, C., Exciton binding energies in carbon nanotubes from two-photon photoluminescence. *Phys Rev B* **2005,** *72* (24).
21. Dukovic, G.; Wang, F.; Song, D. H.; Sfeir, M. Y.; Heinz, T. F.; Brus, L. E., Structural dependence of excitonic optical transitions and band-gap energies in carbon nanotubes. *Nano Lett* **2005,** *5* (11), 2314-2318.
22. Manzoni, C.; Gambetta, A.; Menna, E.; Meneghetti, M.; Lanzani, G.; Cerullo, G., Intersubband exciton relaxation dynamics in single-walled carbon nanotubes. *Phys Rev Lett* **2005,** *94* (20).
23. Huang, L.; Pedrosa, H. N.; Krauss, T. D., Ultrafast Ground-State Recovery of Single-Walled Carbon Nanotubes. *Phys Rev Lett* **2004,** *93* (1), 017403.
24. Mehlenbacher, R. D.; Wu, M. Y.; Grechko, M.; Laaser, J. E.; Arnold, M. S.; Zanni, M. T., Photoexcitation Dynamics of Coupled Semiconducting Carbon Nanotube Thin Films. *Nano Lett* **2013,** *13* (4), 1495-1501.
25. Ruzicka, B. A.; Wang, R.; Lohrman, J.; Ren, S. Q.; Zhao, H., Exciton diffusion in semiconducting single-walled carbon nanotubes studied by transient absorption microscopy. *Phys Rev B* **2012,** *86* (20).
26. Siitonen, A. J.; Tsyboulski, D. A.; Bachilo, S. M.; Weisman, R. B., Surfactant-Dependent Exciton Mobility in Single-Walled Carbon Nanotubes Studied by Single-Molecule Reactions. *Nano Lett* **2010,** *10* (5), 1595-1599.
27. Gokus, T.; Cognet, L.; Duque, J. G.; Pasquali, M.; Hartschuh, A.; Lounis, B., Mono- and Biexponential Luminescence Decays of Individual Single-Walled Carbon Nanotubes. *J Phys Chem C* **2010,** *114* (33), 14025-14028.
28. Cognet, L.; Tsyboulski, D. A.; Rocha, J. D. R.; Doyle, C. D.; Tour, J. M.; Weisman, R. B., Stepwise quenching of exciton fluorescence in carbon nanotubes by single-molecule reactions. *Science* **2007,** *316* (5830), 1465-1468.
29. Crochet, J. J.; Duque, J. G.; Werner, J. H.; Doorn, S. K., Photoluminescence imaging of electronic-impurity-induced exciton quenching in single-walled carbon nanotubes. *Nat Nanotechnol* **2012,** *7* (2), 126-132.
30. Yoshikawa, K.; Matsuda, K.; Kanemitsu, Y., Exciton Transport in Suspended Single Carbon Nanotubes Studied by Photoluminescence Imaging Spectroscopy. *J Phys Chem C* **2010,** *114* (10), 4353-4356.
31. Durgun, E.; Dag, S.; Ciraci, S.; Gulseren, O., Energetics and electronic structures of individual atoms adsorbed on carbon nanotubes. *J Phys Chem B* **2004,** *108* (2), 575-582.
32. Duong, D. L.; Lee, I. H.; Kim, K. K.; Kong, J.; Lee, S. M.; Lee, Y. H., Carbon Nanotube Doping Mechanism in a Salt Solution and Hygroscopic Effect: Density Functional Theory. *Acs Nano* **2010,** *4* (9), 5430-5436.
33. Wang, F.; Dukovic, G.; Knoesel, E.; Brus, L. E.; Heinz, T. F., Observation of rapid Auger recombination in optically excited semiconducting carbon nanotubes. *Phys Rev B* **2004,** *70* (24).
34. Matsuda, K.; Inoue, T.; Murakami, Y.; Maruyama, S.; Kanemitsu, Y., Exciton dephasing and multiexciton recombinations in a single carbon nanotube. *Phys Rev B* **2008,** *77* (3).
35. Wang, F.; Wu, Y.; Hybertsen, M. S.; Heinz, T. F., Auger recombination of excitons in one-dimensional systems. *Phys Rev B* **2006,** *73* (24).

36. Crochet, J. J.; Duque, J. G.; Werner, J. H.; Lounis, B.; Cognet, L.; Doorn, S. K., Disorder Limited Exciton Transport in Colloidal Single-Wall Carbon Nanotubes. *Nano Lett* **2012,** *12* (10), 5091-5096.
37. Rajan, A.; Strano, M. S.; Heller, D. A.; Hertel, T.; Schulten, K., Length-dependent optical effects in single walled carbon nanotubes. *J Phys Chem B* **2008,** *112* (19), 6211-6213.
38. Luer, L.; Crochet, J.; Hertel, T.; Cerullo, G.; Lanzani, G., Ultrafast Excitation Energy Transfer in Small Semiconducting Carbon Nanotube Aggregates. *Acs Nano* **2010,** *4* (7), 4265-4273.
39. Crochet, J. J.; Sau, J. D.; Duque, J. G.; Doorn, S. K.; Cohen, M. L., Electrodynamic and Excitonic Intertube Interactions in Semiconducting Carbon Nanotube Aggregates. *Acs Nano* **2011,** *5* (4), 2611-2618.
40. Delaney, P.; Choi, H. J.; Ihm, J.; Louie, S. G.; Cohen, M. L., Broken symmetry and pseudogaps in ropes of carbon nanotubes. *Nature* **1998,** *391* (6666), 466-468.
41. Topinka, M. A.; Rowell, M. W.; Goldhaber-Gordon, D.; McGehee, M. D.; Hecht, D. S.; Gruner, G., Charge Transport in Interpenetrating Networks of Semiconducting and Metallic Carbon Nanotubes. *Nano Lett* **2009,** *9* (5), 1866-1871.
42. Yang, Z.; Liao, A.; Pop, E., Multiband Mobility in Semiconducting Carbon Nanotubes. *Electron Device Letters, IEEE* **2009,** *30* (10), 1078-1080.
43. Nugraha, A. R. T.; Saito, R.; Sato, K.; Araujo, P. T.; Jorio, A.; Dresselhaus, M. S., Dielectric constant model for environmental effects on the exciton energies of single wall carbon nanotubes. *Applied Physics Letters* **2010,** *97* (9), 091905-3.
44. Nelson, J., *The physics of solar cells*. Imperial College Press: London, 2003; p xix, 363 p.
45. Benedict, L. X.; Louie, S. G.; Cohen, M. L., Static polarizabilities of single-wall carbon nanotubes. *Phys Rev B* **1995,** *52* (11), 8541-8549.
46. Arnold, M. S.; Green, A. A.; Hulvat, J. F.; Stupp, S. I.; Hersam, M. C., Sorting carbon nanotubes by electronic structure using density differentiation. *Nat Nano* **2006,** *1* (1), 60-65.
47. Nessim, G. D.; Hart, A. J.; Kim, J. S.; Acquaviva, D.; Oh, J.; Morgan, C. D.; Seita, M.; Leib, J. S.; Thompson, C. V., Tuning of Vertically-Aligned Carbon Nanotube Diameter and Areal Density through Catalyst Pre-Treatment. *Nano Lett* **2008,** *8* (11), 3587-3593.
48. Fischer, J. E.; Zhou, W.; Vavro, J.; Llaguno, M. C.; Guthy, C.; Haggenmueller, R.; Casavant, M. J.; Walters, D. E.; Smalley, R. E., Magnetically aligned single wall carbon nanotube films: Preferred orientation and anisotropic transport properties. *J Appl Phys* **2003,** *93* (4), 2157-2163.
49. Lu, M.; Jang, M.-W.; Haugstad, G.; Campbell, S. A.; Cui, T., Well-aligned and suspended single-walled carbon nanotube film: Directed self-assembly, patterning, and characterization. *Applied Physics Letters* **2009,** *94* (26), 261903-3.
50. Luer, L.; Hoseinkhani, S.; Polli, D.; Crochet, J.; Hertel, T.; Lanzani, G., Size and mobility of excitons in (6, 5) carbon nanotubes. *Nat Phys* **2009,** *5* (1), 54-58.
51. Hertel, T.; Himmelein, S.; Ackermann, T.; Stich, D.; Crochet, J., Diffusion Limited Photoluminescence Quantum Yields in 1-D Semiconductors: Single-Wall Carbon Nanotubes. *Acs Nano* **2010,** *4* (12), 7161-7168.
52. Anderson, M. D.; Xiao, Y.-f.; Fraser, J. M., First-passage theory of exciton population loss in single-walled carbon nanotubes reveals micron-scale intrinsic diffusion lengths. *Phys Rev B* **2013,** *88* (4), 045420.
53. Hirori, H.; Matsuda, K.; Miyauchi, Y.; Maruyama, S.; Kanemitsu, Y., Exciton Localization of Single-Walled Carbon Nanotubes Revealed by Femtosecond Excitation Correlation Spectroscopy. *Phys Rev Lett* **2006,** *97* (25), 257401.
54. Dürkop, T.; Getty, S. A.; Cobas, E.; Fuhrer, M. S., Extraordinary Mobility in Semiconducting Carbon Nanotubes. *Nano Lett* **2003,** *4* (1), 35-39.

55. Gabor, N. M.; Zhong, Z. H.; Bosnick, K.; McEuen, P. L., Ultrafast Photocurrent Measurement of the Escape Time of Electrons and Holes from Carbon Nanotube p-i-n Photodiodes. *Phys Rev Lett* **2012,** *108* (8).